



HAL
open science

Defect microstructure of a Ti64 alloy under Ti²⁺ ion irradiation. Influence of dose and temperature

Sylvie Doriot, Joel Malaplate, Benoit Arnal, France Dalle

► To cite this version:

Sylvie Doriot, Joel Malaplate, Benoit Arnal, France Dalle. Defect microstructure of a Ti64 alloy under Ti²⁺ ion irradiation. Influence of dose and temperature. Journal of Nuclear Materials, 2023, 583, pp.154528. 10.1016/j.jnucmat.2023.154528 . cea-04123761

HAL Id: cea-04123761

<https://cea.hal.science/cea-04123761>

Submitted on 9 Jun 2023

HAL is a multi-disciplinary open access archive for the deposit and dissemination of scientific research documents, whether they are published or not. The documents may come from teaching and research institutions in France or abroad, or from public or private research centers.

L'archive ouverte pluridisciplinaire **HAL**, est destinée au dépôt et à la diffusion de documents scientifiques de niveau recherche, publiés ou non, émanant des établissements d'enseignement et de recherche français ou étrangers, des laboratoires publics ou privés.

**DEFECT MICROSTRUCTURE OF A Ti64 ALLOY UNDER TI²⁺ ION
IRRADIATION. INFLUENCE OF DOSE AND TEMPERATURE.**

Sylvie Doriot

Université Paris-Saclay, CEA, Service de Recherche en Matériaux et procédés Avancés, 91191, Gif-sur-Yvette, France
sylvie.doriot@cea.fr

Joël Malaplate

Université Paris-Saclay, CEA, Service de Recherche en Matériaux et procédés Avancés, 91191, Gif-sur-Yvette, France
joel.malaplate@cea.fr

Benoît Arnal

Université Paris-Saclay, CEA, Service de Recherche en Matériaux et procédés Avancés, 91191, Gif-sur-Yvette, France
benoit.arnal@cea.fr

France Dalle

Université Paris-Saclay, CEA, Service de Recherche en Matériaux et procédés Avancés, 91191, Gif-sur-Yvette, France.
france.dalle@cea.fr

Corresponding author: Sylvie Doriot (sylvie.doriot@cea.fr)

ABSTRACT

The present paper focuses on the microstructural changes in Ti64 alloy after irradiation. The titanium alloys allow a significant decrease in activation and mass with a similar mechanical strength and a similar corrosion resistance than 304 stainless steels, widely used for core internal structures of Pressurized Water Reactors. The use of titanium alloys could be therefore a significant improvement for reactor exploitation and decommissioning. The nature, size and density of the radiation-induced defects are likely to be important parameters governing the in-reactor behavior of the material. The aim of the study was to devise new achievements in thin foil preparation and Transmission Electron Microscopy (TEM) imaging in order to accurately identify and quantify the Ti64 irradiation defects, at temperatures representative of irradiation temperatures in a reactor. The method to image and count the precipitates was developed with samples irradiated by ions at the temperature of 600°C. Indeed, the microstructure of the sample irradiated at 600°C was characterized by a low density of tangled dislocations, and big precipitates, that were easily evidenced. Then the process was applied in samples irradiated with ions at 430°C and 300°C characterized by a microstructure of tangled dislocations, loops and small precipitates. In 430°C irradiation condition, the measurement in dark field with a $B\sim[11-23]_{\alpha}$ orientation and with a high magnification micrograph provided similar results than Atom Probe Tomography (APT) analyses. In irradiation condition at 300°C, the precipitates were imaged by TEM as soon as the dose of 1 dpa. However they were not observed at the dose of 0.4 dpa. The precipitates were so small and their density was so high that the measurement by TEM was very imprecise and APT analyses were needed. The results of this microstructural analysis allowed a discussion on the nucleation mechanism of the irradiation defects in Ti64 alloys.

Keywords: titanium alloy, irradiation defects, dislocation loops, precipitates, transmission electron microscopy, charged particle irradiation, atom probe tomography.

1. INTRODUCTION

Titanium alloys could be good candidate materials for core reactor internal of Pressurized Water Reactors (PWR) as outlined in a previous study [1]. They may facilitate maintenance operations, dismantling and recycling facilities [2]. Indeed it appeared that titanium alloys allow a significant decrease in activation and mass with a similar mechanical strength and a comparable corrosion resistance than the 304 Stainless Steel, widely used for the core internal structures in PWR. In particular, the chemical elements within titanium alloys are far more favorable from activation point of view than ones in 304 steels. The nature, size and density of the radiation-induced defects are likely to be important parameters governing the in-reactor material behavior. Consequently, for a better understanding of the mechanical behavior under irradiation, it appeared necessary to identify and quantify these defects carefully after irradiation. Because Ti64 is a widely used industrial titanium alloy, the present study focused on the microstructural changes in a ($\alpha+\beta$) Ti64 alloy after irradiation.

The tensile behavior of the ($\alpha+\beta$) Ti64 alloy is known to evolve noticeably after neutron irradiation, not only at low irradiation temperatures ($\leq 250^\circ\text{C}$) [3,4], but also at higher irradiation temperatures near 350°C [5]. The irradiation at 350°C caused a very substantial amount of hardening in the ($\alpha+\beta$) Ti64 alloy and a decrease in the total and uniform elongation, while the α titanium alloys were not strongly affected [4,6]. The irradiation at low temperatures induced the occurrence of small numerous irradiation defects (dislocation loops, black dots) in both α and ($\alpha+\beta$) alloys [7]. The hardening observed in the ($\alpha+\beta$) Ti64 alloy after irradiation at 350°C was said to be mainly related to the radiation-induced precipitation that occurred at doses as low as 0.3 dpa [8,9] in this alloy.

In the view of avoiding long and costly irradiations in nuclear reactors, ion irradiations were managed in this study to emulate neutron irradiations, leading to non-radioactive samples that are easier to prepare and to analyze. Although the dose-rates and the interactions between the particles and the material are known to be very different in the case of neutron or ion irradiations [10], vanadium-rich β precipitates were evidenced in the α phase of Ti64 alloys [1,11,12,13,14,15] after heavy ion irradiations at temperatures ranging from 300°C to 650°C . Quantitative measures (length, number density, chemical composition), in short supply, were mostly carried out from samples irradiated at 500°C . At this irradiation temperature the radiation-induced precipitates measured more than 50 nm in length and the $\langle a \rangle$ -loop contrast had almost disappeared. Thus, it was easy to evidence the precipitates by Transmission Electron Microscopy (TEM). For microstructures representative of the microstructure observed after neutron irradiation in a reactor, with tangled contrasts of $\langle a \rangle$ - loops and smaller precipitates [7,8], Atom Probe Tomography (APT) highlighted a high quantity of these particles at an irradiation temperature as low as 300°C [1], not evidenced by TEM. The radiation-induced precipitates were resolved on the TEM micrographs at the irradiation temperature of 430°C [15] but where counted much less numerous with TEM than with APT analyses [1].

The aim of the present study was to devise new achievements in thin foil preparation and TEM imaging methods in order to accurately identify and quantify the defects (especially the radiation-induced precipitates), at temperatures representative of irradiation temperatures in a reactor. The method to image the precipitates was developed with samples irradiated by ions at the temperature of 600°C , where the irradiation-induced precipitates were easy to evidence. Then, thanks to this method, the irradiation defects were carefully characterized after ion irradiations at temperatures representative of in reactor conditions. For this purpose, ion irradiations were performed in JANNuS French platform at 600°C and 300°C . Samples irradiated previously at 430°C [1] were observed and quantitatively measured again, in this study, to serve as a comparison with the previous method. The results of this microstructural

analyze allowed a discussion on the nucleation and growth mechanism of the irradiation defects in the Ti64 alloy.

2. MATERIAL AND EXPERIMENTAL PROCEDURES

2.1. Material of the study

The considered material was a Ti64 (grade 5) alloy with a duplex microstructure that consisted of both some nodular (α_p) and some lamellar (α_λ) α phase surrounded by some β phase, already described in ref. [1]. This material was provided by TIMET Savoie, France, as a bar of 100 mm in diameter. The nominal chemical composition of the as-received material is given in Table 1 [1].

Table 1. Nominal chemical composition of the Ti64 alloy (wt.%).

Elements	Ti	Al	V	Fe	C	O	N
	bal.	6.47	4.04	0.14	0.009	0.18	0.004

After a hot forming in the $(\alpha+\beta)^1$ domain, the Ti64 alloy was annealed for 2h at 730°C and subsequently air cooled. This led to nodular particles α_p with a mean equivalent diameter of about 10 μm . The apparent size of the α_λ lamellar phase is about several micrometers in thickness and 10 μm in length. The cooling rate after the annealing was low (several bars were cooled together), thus no α' phase was expected. The surface fraction of the β phase was measured before irradiation by BSE-SEM micrographs to be about 10% [1] (Figure 1).

The un-irradiated material was characterized by TEM elsewhere [1]. In the nodular α_p phase, it was possible to encounter dislocations forming sub-grain boundaries (Figure 2b). These sub-grain boundaries formed laths with about 300 – 500 nm in width. They were already observed in the literature [16,17,18], and notably by Leguey et al. in a Ti64 alloy produced by TIMET in a similar way [16]. In these sub-grains, and also, in the lamellar phase, small arrays of short dislocations were observed (Figure 2). The linear dislocation density was counted 10 times higher in the α_λ and in the (α_p + sub grain) phase than in the nodular grains (Table 2).

Table 2. Linear dislocation density in the as received state

	<a> dislocations m/m ³
α_p	$(7.05\pm 4.5)\times 10^{12}$
α_p + Sub grains	$(6.6\pm 1.9)\times 10^{13}$
α_λ	$(5.7\pm 2.7)\times 10^{13}$

¹ The β transus temperature of this alloy is 1000 \pm 5°C.

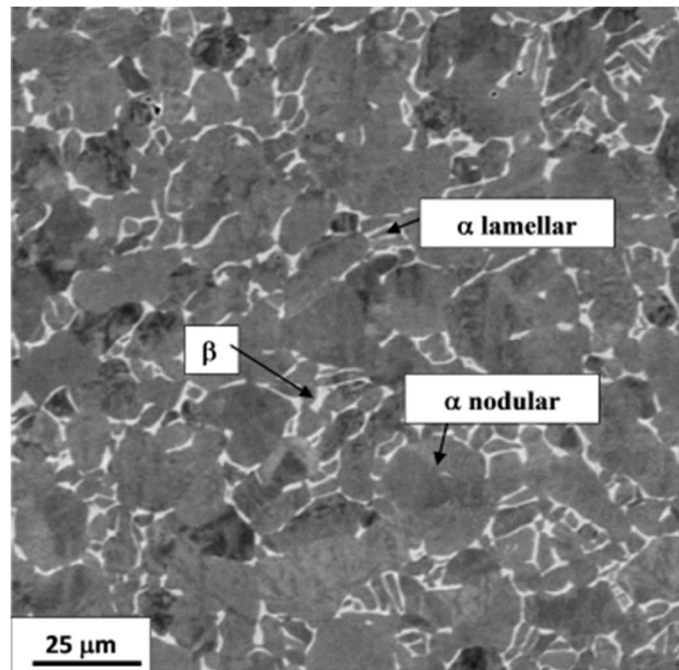


Figure 1. (from ref. [1]). BSE-SEM micrograph of the as-received Ti64 titanium alloy (the α and β phases appear in grey and white, respectively).

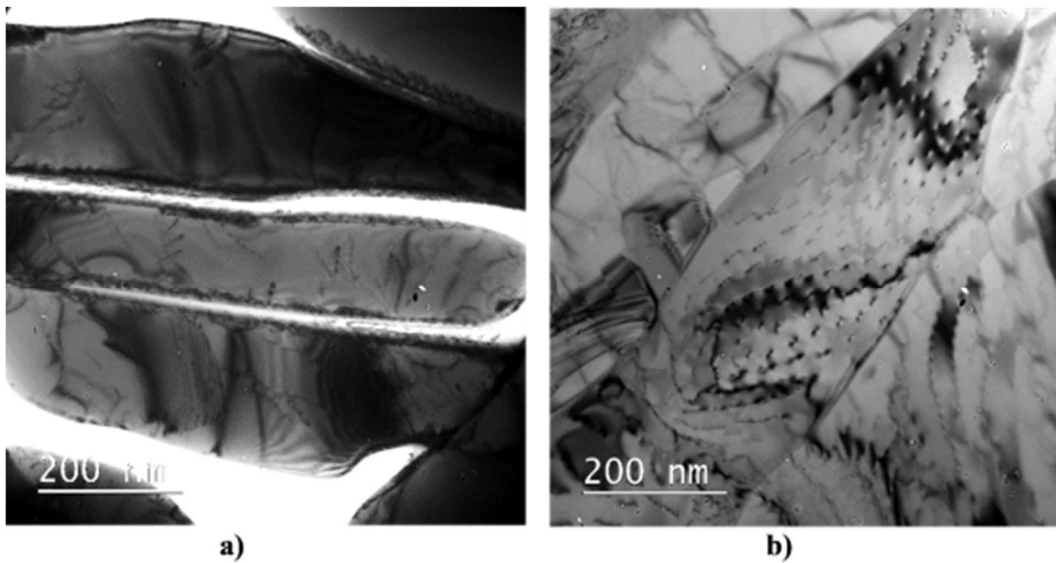


Figure 2. Small arrays of short dislocations observed, a) in the lamellar phase α_l , b) in the sub-grains of the nodular phase α_p + sub grains.

2.2. Irradiation conditions

Disk specimens with a diameter of 3 mm and a thickness of 100 μm were irradiated at 600°C, in a similar way as described in ref. [19] and with the same sample-holder. Then irradiation at 300°C was devoted to both future nano-indentation measurements and TEM observations. Thus, a second sample-holder was used for this 300°C irradiation with a 2 x 0.5x 0.15 cm platelet and three thin disk specimens (diameter of 3 mm and thickness of 100 μm , Figure 3). A mask enabled to provide several doses in the same irradiation experiment: the displacements of the mask during the irradiation exposed progressively to the irradiation different areas of the sample holder. Five different areas with five different doses can be distinguished in the platelet (un-irradiated, 0.4 dpa, 1 dpa, 1.5 dpa, 2.3 dpa). The respective doses of the three irradiated disks were 0.4 dpa, 1 dpa and 1.5 dpa. As seen in Figure 3, a CP Ti (not studied here) was irradiated simultaneously.

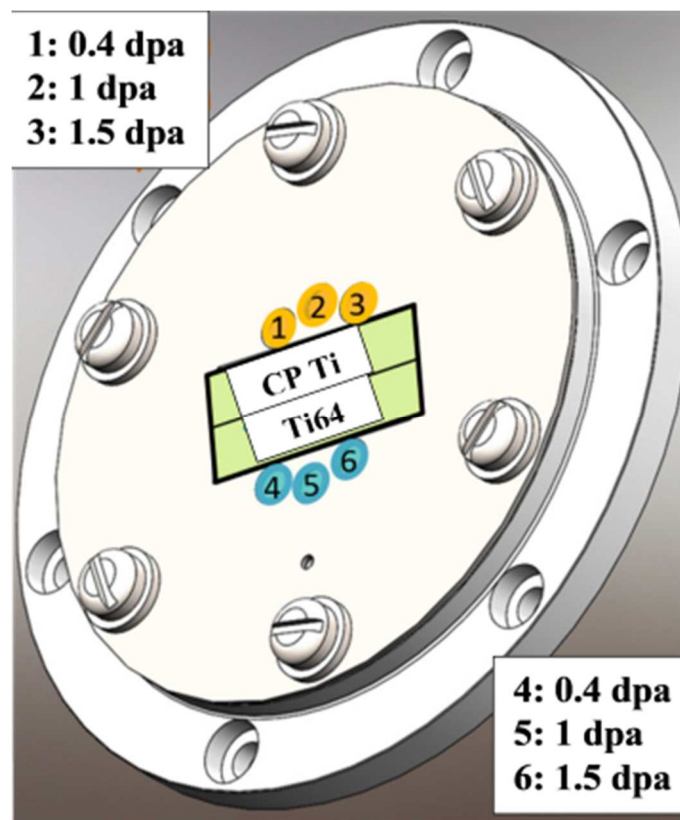


Figure 3. Heating sample holder with nano-indentation platelets and TEM thin foils.

The simulation of the damage and implantation profiles using SRIM (the Stopping and Range of Ions in Matter) software is given in Figure 4 (Kinchin Pease mode, displacement threshold energy $E_d = 25$ eV, target density 4.385 g/cm³, fluence of 1.2×10^{15} atoms/cm²). The damage took place only at the surface of the sample, up to 2 μm deep.

Both irradiations were carried out using Ti^{2+} ions with an energy of 6 MeV and a flux of about 5×10^{11} ions.cm⁻².s⁻¹ (about 1.6×10^{-4} dpa/s), using an aluminum foil degrader (0.8 μm thick). Mansur [20] and Was et al. [10] proposed a formula to determine the shift in temperature to compensate for the damage-rate difference when ion beam irradiation is used for simulating neutron irradiation, as described in ref. [1]. Based on this formula, the 300°C (resp. 430°C) irradiated samples were intended to emulate the microstructure observed after a neutron

irradiation at $\sim 250^{\circ}\text{C}$ (resp. 350°C) with tangled $\langle a \rangle$ -loops and precipitates, as explained previously [1]. Thanks to the high damage-rate, only one or two days were required to reach the expected irradiation doses. Table 3 describes the measured doses, dose-rates and temperatures of the ion irradiations, in the present study. The irradiations were performed in a triple beam chamber using the 2 MV Tandem Pelletron JAPETTM of the JANNuS facility in 2017 [21,22,23]. The sample temperature was measured by a K-type thermocouple welded on the sample surface. The beam current measurements were performed every 10 minutes with a movable device of multi-Faraday cups (going up and down). Both temperature and ion beam offered a good stability during irradiation. The samples irradiated at 430°C at the doses of 0.5 and 2.1 dpa and at 300°C , at the dose of 2.1 dpa, were irradiated previously (in 2013 and 2014) [1].

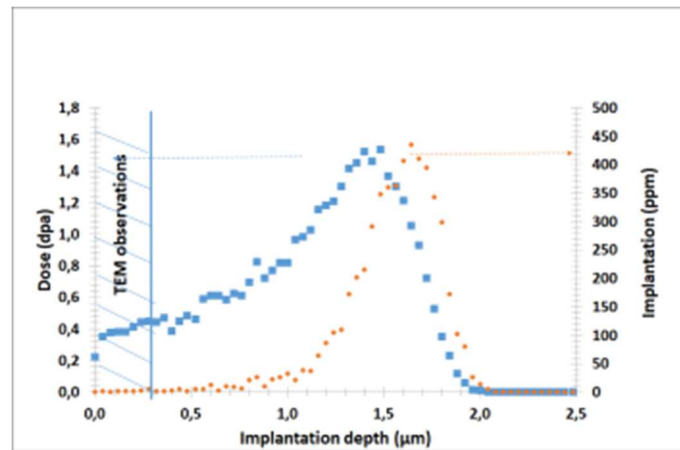


Figure 4. Damage and implantation profile determined from SRIM simulation for irradiations carried out with Ti^{2+} ions at an energy of 6 MeV, using an aluminum foil degrader ($0.8 \mu\text{m}$ thick) in front of the specimen called “0.4 dpa 300°C ”. The part of the profile concerned by TEM observations thanks to electrolytic preparation is hatched and corresponds to a dose of ~ 0.4 dpa.

2.3. Experimental procedures for TEM investigations

Thanks to a specific preparation method explained in ref. [1,19], a thin foil located up to about 200 nm from the irradiated surface (see hatched area in Figure 4) was observed by TEM. The observed area was far from the implanted zone [1], thus no impact of the implanted self-interstitial atoms was expected on the observed defect structures. After electrolytic polishing, some of the samples were additionally cleaned up with argon ions in a Gatan PIPS 2 (model 695) during 5 to 10 mn at 100 eV.

Some cross-sectional samples were also prepared using Focused Ion Beam (FIB) technique. These cross-sectional samples were designed to verify that surface effects did not affect the defect structures. In addition, they aimed at investigating the defect distribution in the depth of the sample. Such samples are essential to check if irradiated depth is consistent with what was predicted by the SRIM calculation and if a difference is observed in the radiation-induced microstructure between the first 200 nanometers (TEM observation) and the deeper irradiated areas that is capital to interpret future nano-indentation results. These thin foils were machined using a double-beam microscope (electronic and Gallium ion beams) Helios Nanolab 650 operating first at 30 kV and then at 2-5 kV for a finishing stage. Figure 5 is a general view of the FIB thin foils prepared in the samples irradiated at the temperature of 430°C (Figure 5a)

and at the dose of ~ 2 dpa, at the temperature of 300°C and at the dose of 0.4 dpa (Figure 5b). As seen in Figure 5, irradiation defects were clearly observable from the top of the thin foils to the depth of about $1.6\ \mu\text{m}$. Thus, the depth of the irradiated area appeared similar but slightly smaller than the depth predicted by the SRIM calculation. The FIB and electrolytic thin foil defects were compared quantitatively. This permitted to check that the irradiation microstructures were the same in both cases and that the FIB preparation did not introduce observable defects in Ti64 alloy.

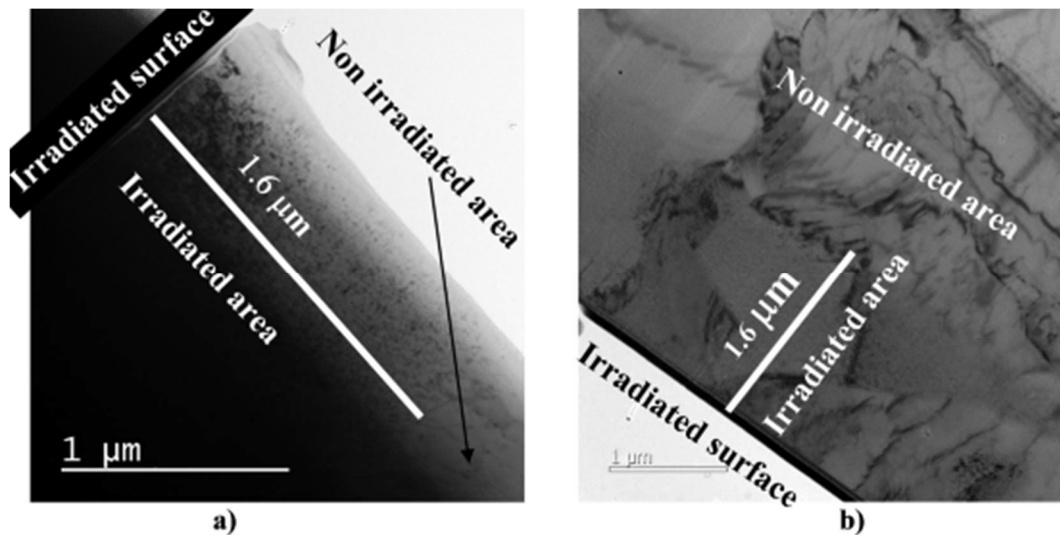


Figure 5. General view of the FIB thin foil. Sample irradiated at, a) 430°C at the dose of 2 dpa, b) 300°C at the dose of 0.4 dpa.

The irradiated thin foils were observed by TEM using a $200\ \text{kV}$ Jeol 2100 microscope. The defect distributions were counted by image analysis, using the Noesis Visilog softwareTM, as explained elsewhere [19]. It can be noticed that the influence of truncation by foil surface can be neglected for $\langle a \rangle$ -type loops and precipitates, because of the small size of these defects compared to the thin foil thickness. The thin foil thickness of the considered location was measured by EELS (Electron Energy Loss Spectroscopy). This technique considers energy distribution of electrons, which have crossed the sample. The thicker the sample, the bigger the incident electron energy loss. Several authors have established the link between the t/λ parameter and the ratio of plasmon peak area and zero loss peak in the energy loss distribution, where t is the thickness of the analyzed zone and λ the mean free path for inelastic scattering [24,25,26,27]. The EELS spectrum was obtained thanks to a Gatan Image Filter (GIF) detector. A t/λ value was automatically extracted by the Gatan Micrograph software. The operating conditions were selected in order to get a collection angle bigger than $100\ \text{mrad}$. In that way the mean free path λ depends on the accelerating voltage of the TEM ($200\ \text{kV}$) and on the mass density of the material only.

A complete characterization of the loops was not carried out, but the presence of $\langle a \rangle$ -loops was checked according to the well-known Burgers vector in hcp metals ($1/3\langle 1-210 \rangle$). The $\langle a \rangle$ -loops were imaged using the reflector $\mathbf{g}=10\text{-}11$, near the prism foil zone axis $\mathbf{B} = [1-210]$ as in ref. [19]. Only $2/3$ of the $\langle a \rangle$ -loops respected the $\mathbf{g}\cdot\mathbf{b} \neq 0$ condition and were visible on the micrographs. Consequently, the number density was obtained by taking into account a corrective factor of $3/2$ to compensate for these missing loops. The measurement was achieved on bright field images only. The magnification of the micrographs was $100\ \text{k}$, with an adding multiplication of about ten by the Orius 200D camera. The choice of a higher magnification

than in ref. [1] permitted to have a better observation of the smaller defects and provided usually a higher density of smaller defects than in ref. [1] for the same irradiation conditions. For all the irradiation conditions, the measurement was carried out on 2 to 4 micrographs that means about 200 defects for $\langle a \rangle$ -loops. The “native”² $\langle a \rangle$ -dislocations were measured on bright field micrographs using reflector $\mathbf{g}=10\text{-}10$ or $\mathbf{g}=10\text{-}11$, near the prism foil zone axis $B = [1\text{-}213]$, at the magnification of 60 k. In addition, the irradiation can create a new $\langle a \rangle$ -dislocation network that was counted in the same micrographs than the $\langle a \rangle$ -loops. As for the $\langle a \rangle$ -loops, the density was given by taking into account a corrective factor of 3/2. The dislocation density ρ was measured thanks to the intercept method with the formula $\rho = N/Lt$ (N =number of intersections between dislocation and drawn straight lines, L total length of drawn straight lines, t thickness of the area). For the precipitate imaging, the observations were conducted in two orientation conditions $B \sim [11\text{-}23]_{\alpha}$ and $\mathbf{g} = 0002_{\alpha}$, for comparison. The measurement was managed on both dark field and bright field imaging and at different magnifications in order to underline the influence of these parameters on the measure accuracy. The precise procedure is detailed in the following.

The standard deviation between the measures in the different areas is indicated by an error bar on the graphs and by uncertainties in the tables. When there is no indication of uncertainty, only one area was counted.

2.4. Experimental procedures for APT

In addition to the TEM observations, atom probe tomography (APT) analyses were carried out in order to obtain chemical and morphological information about the precipitates. Needle tips were prepared by the focused ion beam (FIB) lift-out technique: sections of dimensions $10 \times 2 \times 2 \mu\text{m}$ were extracted from the samples in a FEI Helios Nanolab 650 dual beam FIB machine at CEA, and pieces of sections ($2 \times 2 \times 2 \mu\text{m}$) were mounted onto flat top microtips. Each specimen was then prepared by annular Ga ion milling at CEA. APT experiments were conducted using a LEAP 4000X HR instrument at CEA. The analyses were carried out in the laser evaporation mode ($\lambda = 355 \text{ nm}$) with a 50-60 pJ laser energy, at a temperature of 50 K and with a detection rate of 0.2-0.4 %. Two tips of the material irradiated at $300^{\circ}\text{C} / 0.4 \text{ dpa}$ were analyzed and reached 60 and 143 millions ions (about 0.005 and $0.011 \mu\text{m}^3$ resp.). Similarly, two tips of the material irradiated at $300^{\circ}\text{C} / 1 \text{ dpa}$ provided 61 and 62 millions ions (about $0.005 \mu\text{m}^3$ each). Then the reconstruction of the needle tips was done with the IVAS software, developed by CAMECA. The isosurface method was used for cluster identification: a threshold value is defined for some relevant element content, to separate the clusters from the matrix. For this study, an optimal parameter between 5 and 6 % at vanadium content has been used. The samples irradiated at 430°C and at 300°C at the dose of $\sim 2 \text{ dpa}$ were analyzed elsewhere and previous results were reported here [1]. The needle tips were extracted from the thin foils observed by TEM for an accurate comparison.

2.5. Overview of the analyzed specimens

Table 3 collects and summarizes the information concerning the samples of this study. “New”, for irradiations and analyses indicates that the irradiations and analyses were carried out for the present paper and do not come from ref. [1]. It is worth noticing that the samples irradiated at the temperature of 300°C and at the doses of 0.4, 1 and 1.5 were irradiated simultaneously in the same irradiation campaign. Contrariwise, the sample irradiated at the same temperature of 300°C and at the dose of 2.1 dpa was irradiated previously. It should also be noted that the samples irradiated at the temperature of 430°C (0.5 and 2.1 dpa) were not irradiated simultaneously.

² Dislocations supposed to be already present before irradiation

Table 3. Overview of the specimens analyzed by TEM and APT.

Dose (dpa)	Dose-rate (dpa s ⁻¹)	T _{irr} (°C)	New irradiation	New TEM analyses	New APT analyses	APT analyses from ref. [1]
2.2	1.6x10 ⁻⁴	565-605	X	X		
2.1	1.5x10 ⁻⁴	300-310		X		X(new exploitation)
1.5	1.7x10 ⁻⁴	290-300	X	X		
1	1.6x10 ⁻⁴	290-300	X	X	X	
0.4	1.7x10 ⁻⁴	290-300	X	X	X	
2.1	1.6x10 ⁻⁴	410-430		X		X
0.5	~1x10 ⁻⁴	410-430		X		X

3. EXPERIMENTAL TEM RESULTS ON <a>-TYPE DEFECTS

3.1. Sample irradiated at 600°C 2 dpa

The <a> microstructure of the sample irradiated 2 dpa at 600°C is characterized by a low density of tangled dislocations ($(1.1 \pm 0.1) \times 10^{14} \text{ m}^{-3}$), without any <a>-loops, as seen in Figure 6.

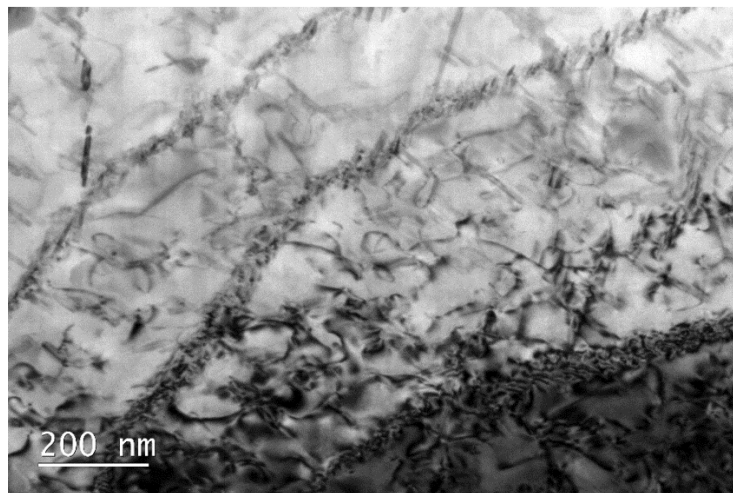


Figure 6. Tangled <a> dislocations in the sample irradiated at the dose of 2 dpa and at the temperature of 600°C.

3.2. Sample irradiated at 430°C, 0.4 and 2 dpa

The <a>-type microstructure of the samples irradiated at 430°C looked similar for both doses (0.4 and 2 dpa) and consisted of a tangled dislocation network associated with dislocation loops

(Figure 7). The density of $\langle a \rangle$ -loops was so high that the dislocation network was hardly visible and cannot be separated from the $\langle a \rangle$ -dislocation contrast for the measurement of the $\langle a \rangle$ -defect linear density (Table 4). With a FIB preparation, the better quality of the thin foil permitted a better appreciation of the $\langle a \rangle$ -loops versus other objects as oxidation contamination or precipitates. This can explain the differences in size and density of the $\langle a \rangle$ -loops measured in the electrolytic and in the FIB thin foils (Table 4). Despite some discrepancy due to the uncertainty of the measure, the quantitative measurement confirmed the similarity of the microstructure at the dose of 0.4 dpa compared to the dose of 2 dpa, with a main diameter of the $\langle a \rangle$ -type loops of about 14 nm and a number density of about $1 \times 10^{22} \text{ m}^{-3}$ (Table 4). The linear density of the $\langle a \rangle$ microstructural defects appeared very high ($\sim 10^{15} \text{ m/m}^3$) compared to the $\langle a \rangle$ -dislocation linear density before irradiation ($\sim 10^{13} \text{ m/m}^3$). For comparison, the linear density of $\langle a \rangle$ -loops was deduced from the density and size of the loops to be about 10^{14} m/m^3 .

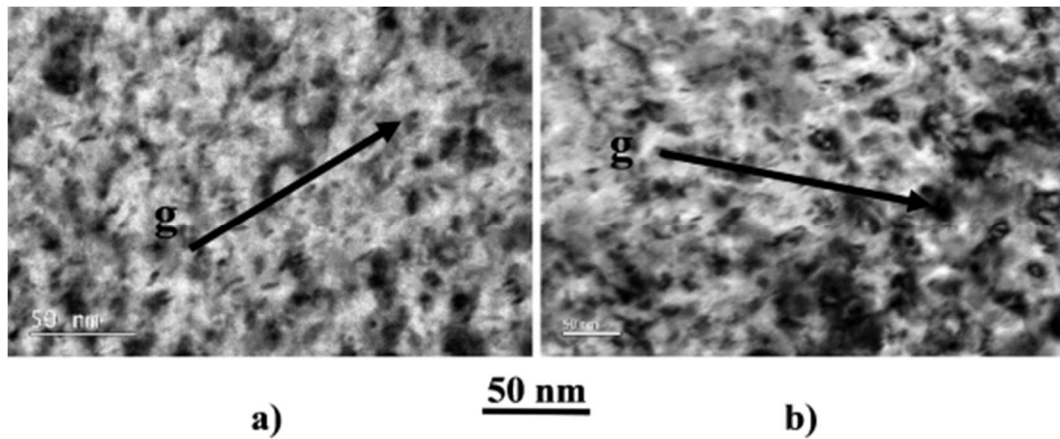


Figure 7. $\langle a \rangle$ -loops and black dots after irradiation at 430°C, $g=10-11 \text{ B} \sim [1-210]$, a) 2.1 dpa, b) 0.4 dpa.

Table 4. Results of the measurement of the $\langle a \rangle$ defects in the samples irradiated at 430°C (dl = linear density, ϕ_m = main diameter, d = number density, V=analysed volume)

Dose (dpa)	Tangled $\langle a \rangle$ -dislocations and loops, dl (10^{14} m/m^3)	ϕ_m (nm)	d ($\times 10^{22} \text{ m}^{-3}$)	V (m^3)
2	7.0 ± 0.4	8 ± 1	1.9 ± 0.1	1.3×10^{-20}
2 (FIB thin foil)	10	14 ± 3	0.9 ± 0.1	1.9×10^{-20}
0.4	8.4 ± 1.1	13 ± 3	2.0 ± 0.6	1.6×10^{-20}

3.3. Samples irradiated at 300°C

In the sample irradiated at 300°C at the dose of 0.4 dpa, the grey contrast distinctive of the irradiated materials was observable in Figure 8a, but the native microstructure (dislocations, sub-grains, laths) was still present. The linear density of the native dislocations was measured similar to the linear density of the dislocations in the un-irradiated specimen

(Table 2 and 5). At the dose of 1 dpa, this native microstructure was less observable (Figure 8b) and almost disappeared at the dose of 1.5 dpa (Figure 10c). These pictures are representative of the general trend of the native $\langle a \rangle$ -type microstructure evolution under irradiation.

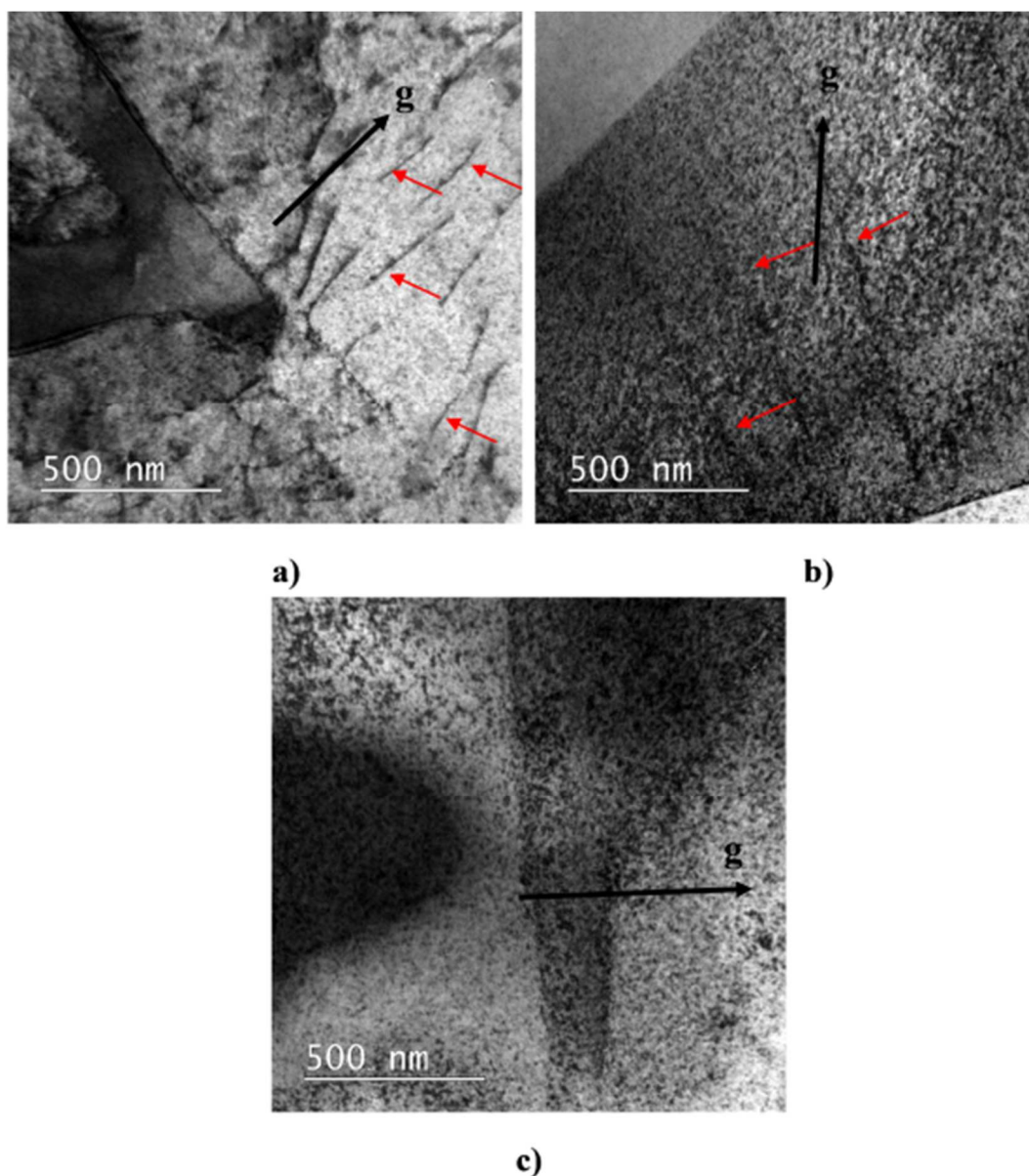


Figure 8. Native $\langle a \rangle$ dislocations in the 300°C irradiated samples, a) 0.4 dpa, $g=1-210$, b) 1 dpa, $g=10-11$, c) 1.5 dpa, $g=1-210$.

In Figure 9 can be observed the $\langle a \rangle$ -type defect microstructure of the samples irradiated at 300°C and at the doses of 0.4, 1, 1.5 and 2 dpa. This microstructure was similar for all the doses and consisted of a tangled dislocation network associated with uniformly spread loops as for the samples irradiated at 430°C. The quantitative measurement (Table 5) confirmed the similarity of the $\langle a \rangle$ -loop density ($d_{\langle a \rangle}$) and mean diameter ($\Phi_{m\langle a \rangle}$) at the four doses with a high density ($0.5-1 \times 10^{23} \text{ m}^{-3}$) of very small loops ($\sim 5 \text{ nm}$) but with a slight tendency for the loops to be more numerous and smaller at low doses. The measurement on the FIB thin foil is consistent with this observation. After a cleaning with PIPS 2, the loops were slightly smaller

likely because the better quality of the thin foil permitted to get a better view of the smaller loops. However the difference between the samples that were cleaned by PIPS 2 and the samples that were not cleaned was not drastic as seen in the measurement of Table 4 and in the micrographs of Figure 9. The total <a>-type defect linear density was measured about twice higher than in the samples irradiated at 430°C. The linear density of <a>-loops deduced from the density and size of the loops is likely twice higher after irradiation at 300°C than after irradiation at 430°C.

Table 5. Results of the measurement of the <a> defects in the samples irradiated at 300°C. (ϕ_m = main diameter, d = number density, V = analyzed volume)

Dose dpa	Native <a> dislocations m/m³	ϕ_m <a> nm	$d_{<a>}$ m⁻³	Total <a>+ dislocation density m⁻²	V(m⁻³)
0.4	$(7\pm 3.6)\times 10^{13}$	4.0 ± 0.1	$(5.7\pm 1.0)\times 10^{22}$	$(1.1\pm 0.2)\times 10^{15}$	1.5×10^{-20}
+PIPS 2		3.8	5.2×10^{22}	1.4×10^{15}	4×10^{-21}
FIB		3.8 ± 0.1	$(1.1\pm 0.5)\times 10^{23}$		1.7×10^{-20}
1	$\sim 2.5\times 10^{13}$	4.6 ± 0.7	$(1.2\pm 0.5)\times 10^{23}$	$(2.2\pm 0.7)\times 10^{15}$	7.1×10^{-21}
+PIPS 2		4.1	6.8×10^{22}	1.2×10^{15}	5.6×10^{-21}
1.5	0	5.9	$(3.5\pm 1.5)\times 10^{22}$	$(1.2\pm 0.2)\times 10^{15}$	1.2×10^{-20}
+PIPS 2	0	4.9	4.9×10^{22}	2.2×10^{15}	3×10^{-21}
2	0	5.0 ± 0.9	$(5.8\pm 1.9)\times 10^{22}$	$(2.4\pm 1.2)\times 10^{15}$	1.9×10^{-20}
+PIPS 2		4.9 ± 0.6	$(8.0\pm 0.9)\times 10^{22}$	$(2.0\pm 0.2)\times 10^{15}$	1.2×10^{-20}

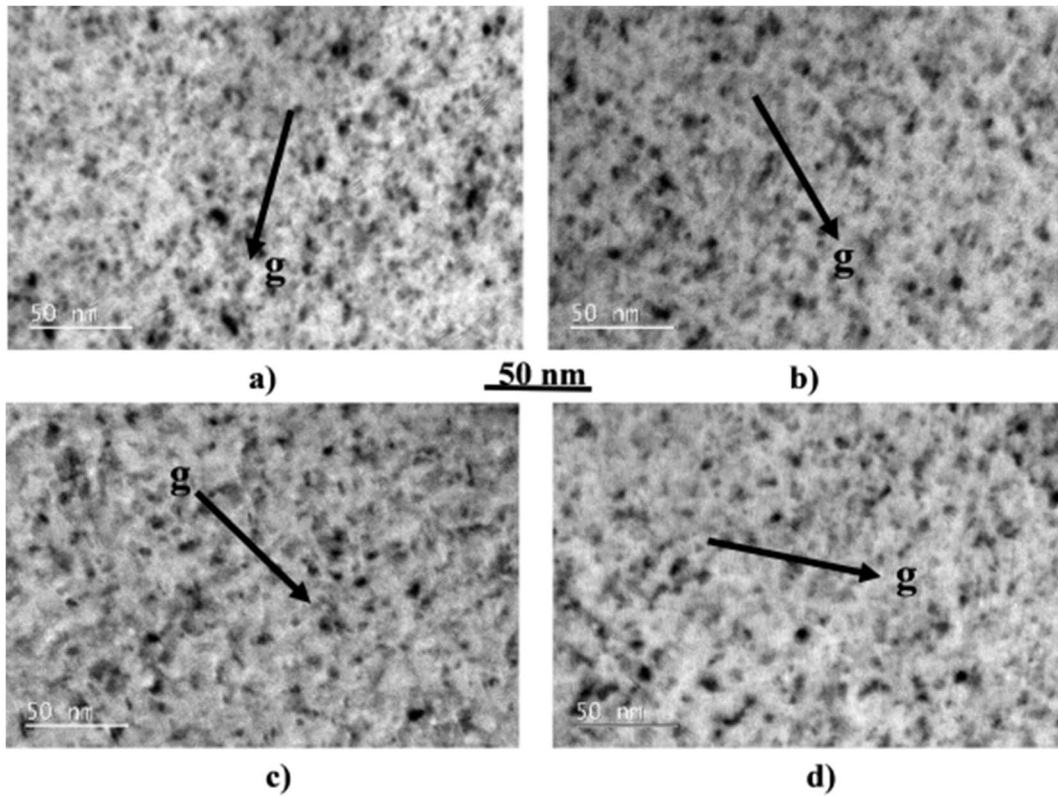


Figure 9. $\langle a \rangle$ -loops and black dots after irradiation at 300°C, $g=10\text{-}11$ $B\sim[1\text{-}210]$, a) 0.4 dpa (without PIPS 2), b) 1 dpa (without PIPS 2), c) 1.5 dpa (with PIPS 2), d) 2 dpa (without PIPS 2).

4. EXPERIMENTAL RESULTS ON RADIATION-INDUCED PRECIPITATES

From the literature, the radiation-induced precipitates were platelet-shaped vanadium-rich β particles and followed the well-known Burgers [28] crystallographic relation with the α matrix [1,11,14,29]

$$(011)_{\beta} // (0001)_{\alpha} \text{ and } [1\bar{1}1]_{\beta} // [11\bar{2}0]_{\alpha}$$

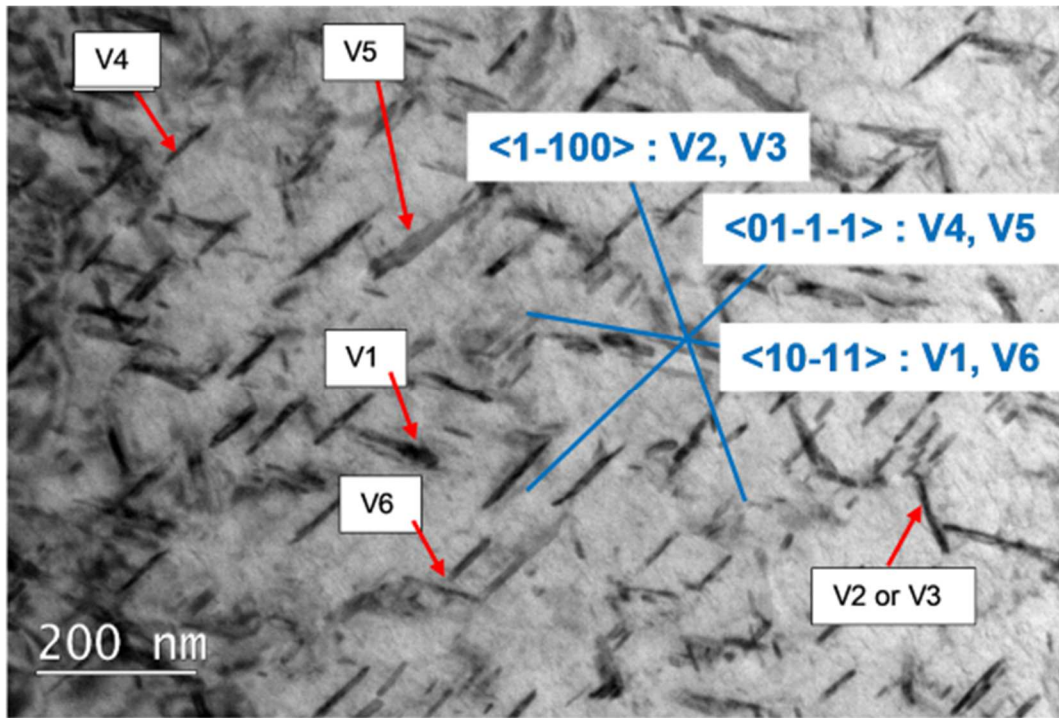
There are three $\mathbf{a}=\langle 1\text{-}210 \rangle_{\alpha}$ directions in the hexagonal base plan and two $\langle 1\text{-}11 \rangle_{\beta}$ directions in the cubic plan $(011)_{\beta}$. Indeed, the Burgers relation induces the occurrence of six equivalent crystallographic orientations or variants, but only three spatial orientations (called S_1 to S_3) of the precipitates were experimentally observed [1]. The six crystallographic variants will be called V_1 to V_6 in the following and will be detailed later in the text.

As said in the introduction, the method to characterize these precipitates was first developed with the sample irradiated at the temperature of 600°C, where the precipitates are easy to observe and measure (§ 4.1). In order to measure and to count the precipitates at lower irradiation temperatures, some adjustments of the method were carried out with the sample irradiated at 430°C, 2 dpa (§ 4.2.). Finally a set of general rules and steps that has been followed to quantify the irradiation-induced precipitates in the present irradiation conditions is summarized in § 4.3. Then, the result of the measurement by TEM and APT is provided.

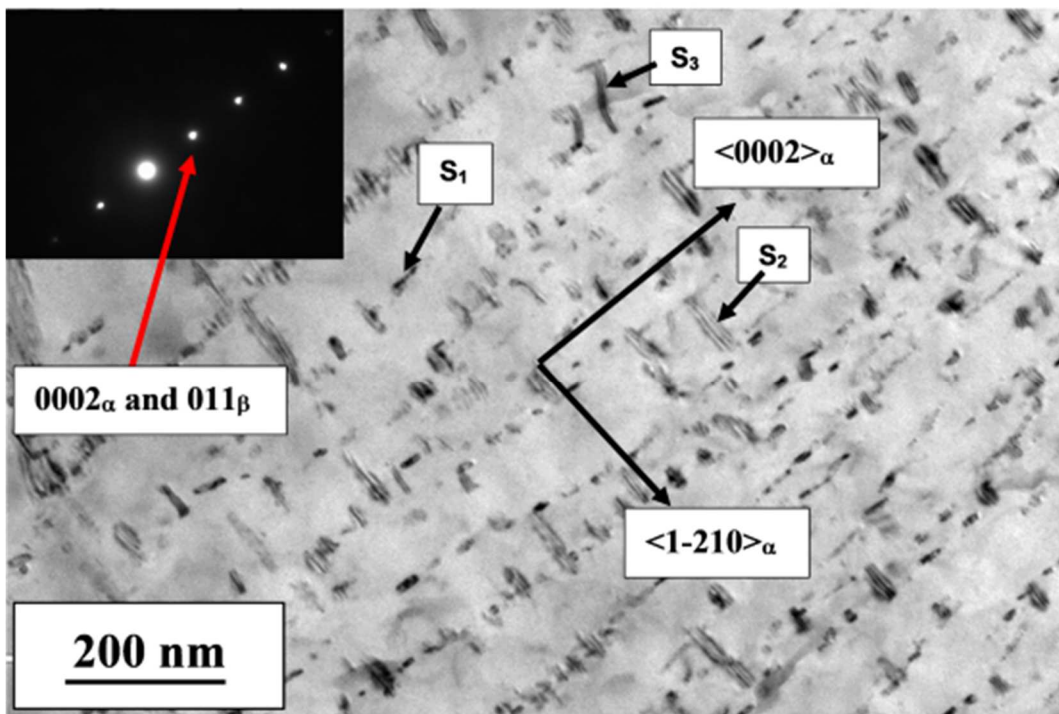
4.1. TEM method development with the sample irradiated 2 dpa at 600°C

After irradiation at 600°C at the dose of 2 dpa, radiation-induced precipitates were easily observed, as expected, with the two observation conditions: $B\sim[1-213]$ (Figure 10a) and $g=0002$ $B\sim[10-10]$ (Figure 10b). No loop contrast was disturbing the precipitate observation. The three expected “spacial variants” were actually in the two micrographs in Figure 10. It is worth noticing that the precipitate aspect and size were different in the two orientation conditions. Indeed it seems essential to count and compare the particles in the same orientation condition in any case. The measurement in the two orientation conditions is compared in the followings (at first $g=0002$, then $B\sim[1-213]$).

All the crystallographic variants have a $[011]_{\beta}$ axis parallel to the $\langle c \rangle$ axis of the hexagon and thus all the variants are in contrast with a $g=0002$ projector. What is more, the $g=0002$ orientation vanishes the unwelcome $\langle a \rangle$ -loop contrast (when there is some). Therefore, the $g=0002$ orientation seemed to be the best orientation to visualize and to count the precipitates. Therefore this orientation is widely used in the literature. However, dark field imaging is not possible in this orientation because the spots 0002_{α} of the matrix and the spot 011_{β} of the precipitates are too close from each other as seen in ref. [11] and in Figure 10b. Furthermore, in this observation condition, the morphologies of the three spatial variants (numbered S_1 to S_3 in Figure 10b) were quite different from each other and could introduce a disparity in the size of the particles. These differences in morphology came from the differences in the observation angles of view. All the particles were platelet-like, but the spatial variant S_1 (in Figure 10b) looked peculiarly fine, compared to the two other spatial variants, and was perpendicular to the $\langle 1-210 \rangle$ direction. It means that its habit plane is probably near the $(1-210)$ crystallographic plane. The large side of the S_1 particles was along the $\langle 0002 \rangle$ direction as seen in Figure 10b. The other spatial variants have probably habit planes near the other $\{1-210\}$ -type planes. There are only three $\{1-210\}$ -type planes in the hexagonal structure that could explain why there are only three spatial variants S_1 to S_3 for six crystallographic variants $V1$ to $V6$.



a)



b)

Figure 10. TEM micrographs of the 600°C, 2.2 dpa irradiated sample, a) B~[1-213] without PIPS 2 (the six crystallographic variants are called V1 to V6 and are detailed in §4.1), b) $g=0002$ B~[10-10], with PIPS 2.

In Figure 11 is compared two areas of the same grain, in the $g=0002$ B~[10-10] orientation, before cleaning with PIPS 2 (Figure 11a) and after cleaning with PIPS 2 (Figure 11b). Marks of contamination (arrowed) are much more apparent before than after the cleaning.

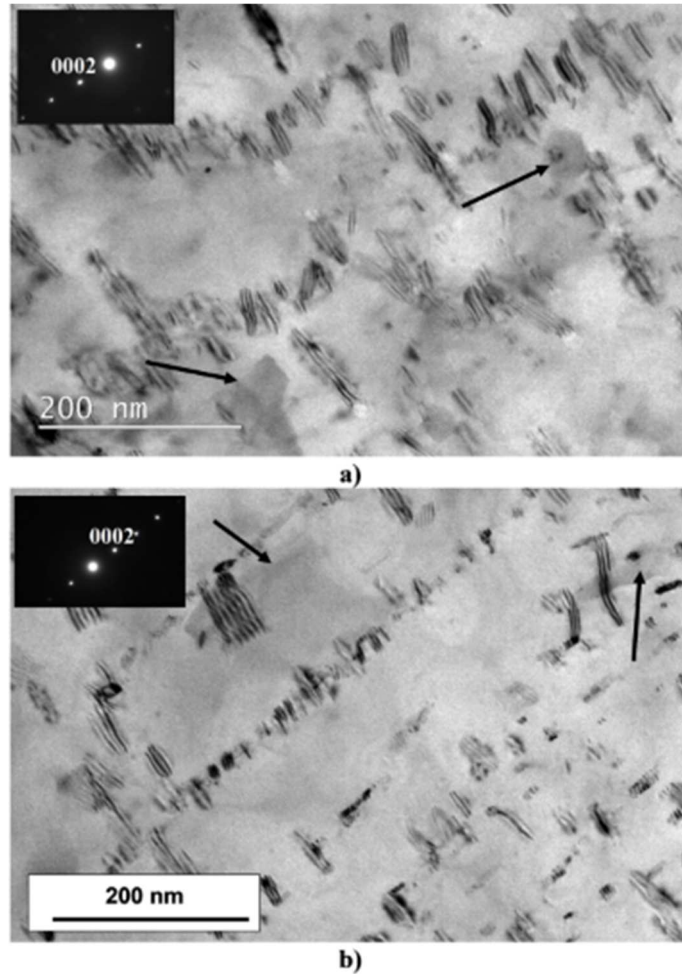


Figure 11. TEM micrographs of the 600°C, 2.2 dpa irradiated sample, $g=0002$ B~[10-10], a) before cleaning with PIPS 2, b) after cleaning with PIPS 2.

The $\langle 11-23 \rangle$ -type zone axes are numerous (there are 6 of them) and the corresponding diffraction patterns are easily recognizable with an almost hexagonal feature (Figure 12). As seen in Figure 13a, in this orientation condition (slightly tilted from the $B = [11-23]$ zone axis), the matrix was out of contrast and thus appeared with a white appearance. This allowed a good visualization of the precipitates. Contrary to the $g=0002$ observation condition, the visual aspects of the variants were similar. The Burgers relationship induces six crystallographic orientation variants V1 to V6 with only three observed spatial orientation S_1 to S_3 separated from a near 60° angle (Figure 10a). This observation leads to an ambiguity on the exact number of observed crystallographic variants in bright field observation. Thus a complete diffraction diagram indexation of the α matrix in the $B = [11-23]_\alpha$ zone axis orientation, with the six superposed β crystallographic variants was conducted in the following.

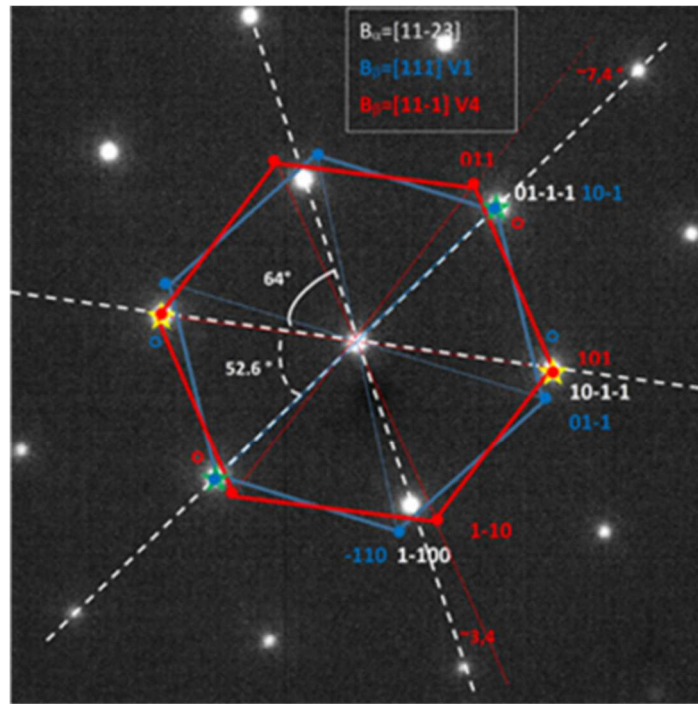
Thanks to stereographic projections, the six crystallographic variants from the Burgers relation (V1 to V6) can be expressed as follow, and the spots corresponding to the six variants were manually reported on the experimental Ti_α matrix diffraction pattern ($B=[11-23]_\alpha$) (Figure 12a): (Relation I)

- (110) $_\beta$ // (0001) $_\alpha$, and $[1-11]_\beta$ // $[-2110]_\alpha$ (V1) ● $[11-2-3]_\alpha \sim 3-4^\circ$ from $[111]_\beta$
 (110) $_\beta$ // (0001) $_\alpha$, and $[-111]_\beta$ // $[-2110]_\alpha$ (V2) ★

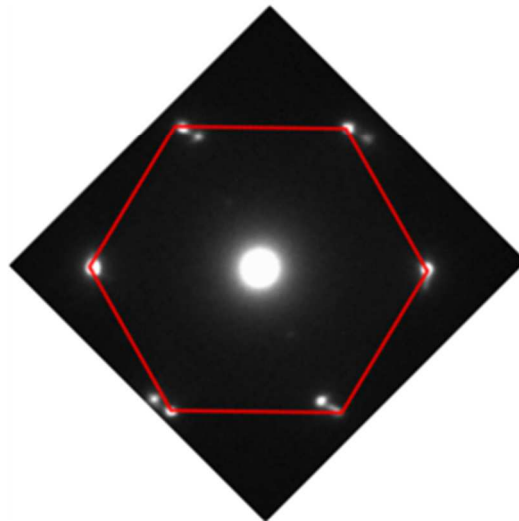
$(110)_\beta // (0001)_\alpha$, and $[1-11]_\beta // [1-210]_\alpha$ (V3)	★	
$(110)_\beta // (0001)_\alpha$, and $[-111]_\beta // [1-210]_\alpha$ (V4)	●	$[11-23]_\alpha \sim 3-4^\circ$ from $[11-1]_\beta$
$(110)_\beta // (0001)_\alpha$, and $[1-11]_\beta // [11-20]_\alpha$ (V5)	○	
$(110)_\beta // (0001)_\alpha$, and $[-111]_\beta // [11-20]_\alpha$ (V6)	○	

Two of the crystallographic variants (V1 and V4) are distant of only few degrees from a zone axis position ($B = \langle 111 \rangle_\beta$), and are represented on Figure 12a by a regular hexagon (resp. blue and red). A 110-type spot of all the crystallographic variants is near a Bragg position in Figure 12a. It appears, in Figure 12a, that the 011 spot of V4, the 01-1 spot of V1 and the 110-type spots of V5 and V6 are easy to use for dark field and are related to one crystallographic variant only. In Figure 12b is observed an experimental diffraction pattern slightly tilted from $B = [11-23]_\alpha$ in order to situate the V4 variant in zone axis position $B = [11-1]_\beta$. The indexation of this experimental diagram confirmed the theoretical position of the V4 variant spots in Figure 12a (the same can be carried out for the V1 variant).

Figure 13 was obtained by slightly tilting the specimen from the $B = [11-23]_\alpha$ axis position around the $\langle 01-1-1 \rangle_\alpha^*$ direction (perpendicular to the (0-1-11) plane). In this orientation, the 011_β spot of V4, and a 110_β -type spot of V5 appeared on both sides of the $01-1-1_\alpha$ spot. Figure 13 provides a dark field image of V4 (Figure 13d) and V5 (Figure 13c) crystallographic variants. The large sides of both V4 and V5 crystallographic variants are along the $\langle 01-1-1 \rangle_\alpha^*$ direction (consistent with a $(-2110)_\alpha$ habit plane). Thus, these two distinct crystallographic variants cannot be distinguished in bright field imaging as seen in Figure 13a and belong to the same spatial variant. In the same way, by slightly tilting the specimen from the $B = [11-23]_\alpha$ axis position around the $\langle 10-1-1 \rangle_\alpha^*$ direction, the V1 and V6 crystallographic variants appeared with the large side along the $\langle 10-1-1 \rangle_\alpha^*$ direction (consistent with a $(1-210)_\alpha$ habit plane). In contrast, the 110-type spots of V2 and V3 crystallographic variants are combined with other variant spots and with matrix spots and cannot be used for a dark field imaging. By deduction from the other variant positions, the large sides of V2 and V3 were along the $\langle 1-100 \rangle_\alpha$ direction (consistent with a $(11-20)_\alpha$ habit plane), (Figure 10a). It is worth noticing that, contrary to V4/V5 and V1/V6 variants, the V2 and V3 variants cannot be distinguished from each other with a dark field imaging in this orientation condition. It is the reason why there are not distinguished from each other in Figure 10a.



a)



b)

Figure 12. Superposition of, a) the experimental matrix and the theoretical precipitate diffraction patterns, $B=[11-23]_{\alpha}$, b) the experimental matrix and precipitate diffraction patterns $B_{\sim} [11-23]_{\alpha}$, $B=[11-1]_{\beta}$ (V4).

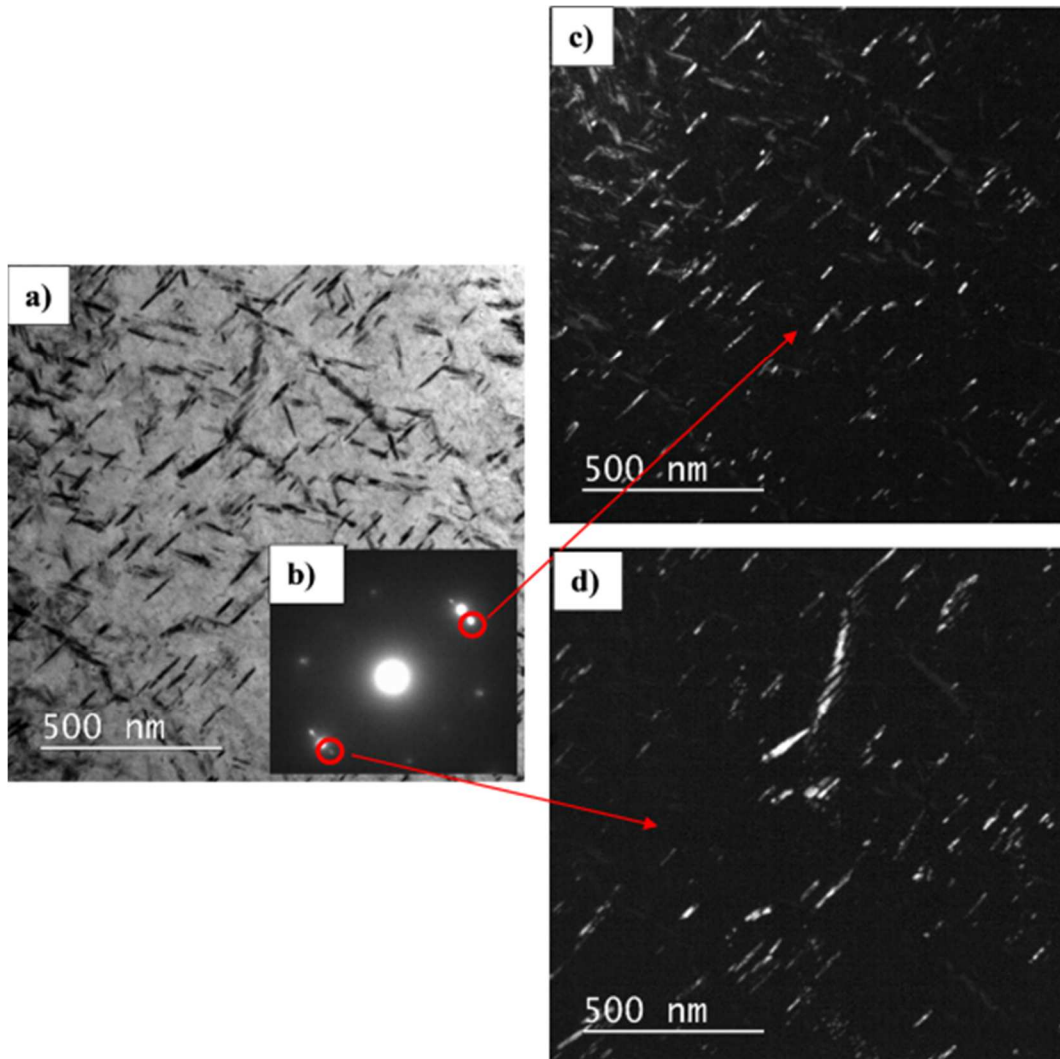


Figure 13. TEM micrographs $B\sim[11-23]_{\alpha}$ $g=01-1-1$, a) bright field, b) diffraction pattern, c) V5 variant in dark field imaging, d) V4 variant in dark field imaging.

A measurement in $B\sim[11-23]_{\alpha}$ orientation was carried out in bright field (V1 variant) and dark field images (V1, V4, V5 variants), in the same area for all, for comparison. In the orientation condition for the measurement of V1, the diffraction pattern ($B\sim[11-23]_{\alpha}$ $g=10-1-1_{\alpha}$) indicated that only the V1 crystallographic variant was in contrast. In addition, the measure provided similar results whatever the variant V1, V4 or V5, and it was assumed that it would be the same for V2, V3 and V6. Thus for both measures in bright (BF) and dark field (DF), the density of the particles was multiplied by 6 in Table 6. In the $g=0002$ orientation, all the crystallographic variants were in contrast and no multiplying was needed. As seen in Table 6, after irradiation at 600°C , the measurement provided similar results whatever the orientation and the imaging mode (DF or BF). However the precipitate medium length appears slightly smaller with a $g=0002$ orientation because the projection of the particles on the observation plane is overall shorter.

Table 6. Measurement of the precipitates in the 2.2 dpa 600°C irradiation conditions (L=length, W=width, d=number density). Bright Field (BF), Dark Field (DF), orientation B~[11-23] in the same area and in orientation g=0002. DF on several grains.

Orientation	condition	L (nm)	W (nm)	dx10 ²¹ m ⁻³
g=10-1-1 B~11-23	DF(V1)	47	14	2.9
g=10-1-1 B~11-23	BF(V1)	48	10	2.6
g=0002	BF	41	11	2.6
g=10-1-1 B~11-23	DF(several grains)	54±8	12±2	2.3±0.6

4.2. Adjustment of the method with the sample irradiated at 430°C at the dose of 2.1 dpa.

Table 7. Measurement of the precipitates in the 2.1 dpa 430°C irradiation conditions (L=length, W=width, d=number density). Comparison Bright Field (BF), Dark Field (DF), Magnification (M) 60K and 100K. Orientations B~[11-23] and g=0002. Comparison with APT.

Orientation	Conditions	M	L (nm)	W (nm)	dx10 ²³ m ⁻³
B~[11-23]	BF	60 K	15.1	3.2	0.9
B~[11-23]	DF	60 K	13.1	2.7	1.0
g=0002	BF	60 K	8	3	0.3
B~[11-23]	BF	100 K	13.1	3.4	1.2
B~[11-23]	DF	100 K	10.6	2.7	1.4
APT [1]			10.2		1.8

In the same way as for irradiation at 600°C, the measurement of the precipitates after irradiation at 430°C, 2 dpa, was carried out in the B~[11-23]_α orientation, in bright field and in dark field imaging, in the same area. This measure was then compared in Table 7 to the result of the measurement in the g=0002 orientation. In addition two different magnifications were used (60 K and 100 K). For this lower irradiation temperature (430°C), the magnification of the picture affected the result of the measure (Table 7). A bigger magnification permitted to see better the smaller precipitates and provided a higher density of smaller particles. The density of the detected precipitates dropped down drastically with a g=0002 orientation compared to the B~[11-23]_α orientation (Tables 7). In agreement with the measurement after irradiation at the temperature of 600°C, the precipitates appear shorter with a g=0002 orientation. Finely, there were 10 to 15 % precipitates less in bright field than in dark field imaging measurement. It is worth noticing that the result with a DF images in B~[11-23] orientation with a high

magnification is the nearest result to that of the APT measures [1]. Thus in 430°C irradiation condition, with tangled contrasts of <a>-type loops and smaller precipitates, the measurement in the B~[11-23]_α orientation with a high magnification micrograph appeared to be highly more accurate than a lower magnification and a g=0002 orientation.

4.3. Application to the measure of precipitates after irradiation at 430°C and 300°C

Thanks to the foregoing studies, general rules and steps for the measurement of the radiation-induced precipitates after low irradiation temperatures can be proposed. The measurement should be carried out in several areas and in several grains for a better statistic.

- 1st step: a grain with a near B~[11-23]_α orientation is requested (Figure 12)
- 2nd step: a slight tilt around a <10-11>* direction is needed to reinforce the 101 spots of the beta precipitates on one or both sides of the 10-11 spot of the matrix (Figure 13)
- 3rd step: one of the 101 spots of the precipitates (near the 10-11 spot of the matrix) is then selected for a DF imaging with a high magnification (Figures 14 and 15 are representatives of the micrographs used for the measurement). Only one crystallographic variant is enlightened.
- 4th step: the thickness of the studied area is measured by EELS (§ 2.3.). A thickness of about 100 nm seems to be a good compromise between statistic consideration and visualization.
- 5th step: the precipitates are manually selected and drawn thanks to a graphic tablet, and then automatically counted and measured by the Noesis Visilog softwareTM (Figure 15). The density is finally multiply by six to take into account the 6 variants.

In Table 8 is collected the result of the TEM measurement on several micrographs for doses 0.4 and 2 dpa, at the irradiation temperature of 430°C. It appears that the precipitate density and size are similar at both doses, with a medium length of about 10 nm, a medium width of about 3 nm, and a density of about $1.5 \times 10^{23} \text{ m}^{-3}$. The quantitative measurement of the particles in the FIB thin foil at different depths, not reported here, was similar to what was measured with the thin foils prepared with an electrolyte (Table 8). It indicated after irradiation at 430°C similar density and size of the defects all along the irradiated area. This is consistent with a saturation of the defects as soon as 0.4 dpa at this irradiation temperature, as seen before in [1]. The comparison with previous APT measurement [1] shows the coherency of both methods.

Table 8. Measurement of the precipitates after irradiation at the temperature of 430°C, in several grains (L=length, W=width, d=number density), in Dark Field (DF), Magnification 100 K. Orientation B~[11-23].

Dose (dpa)	L (nm)		W (nm)		d x10 ²³ m ⁻³		V (m-3)
	TEM	APT[1]	TEM	TEM	APT[1]	TEM	
2	11.0±0.9	10.2±5.3	2.8±0.05	1.3±0.3	1.8	2.9x10 ⁻²⁰	
0.4	15.6±0.1	10.6±8.0	4.1±0.1	1.7±0.1	1.3	8.7x10 ⁻²¹	

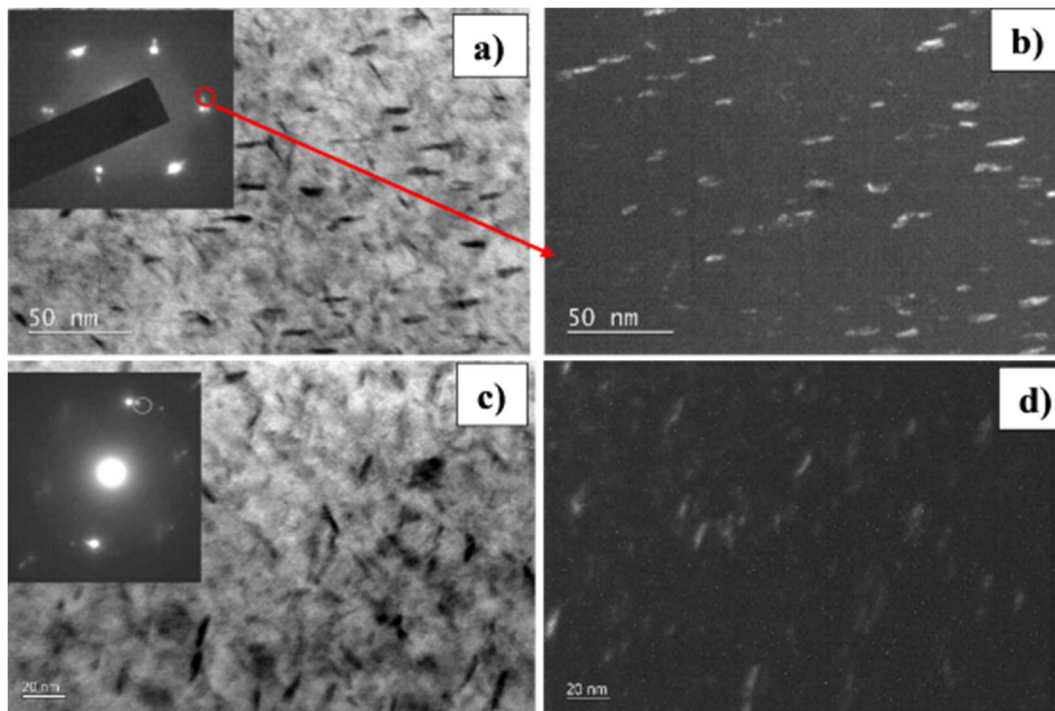


Figure 14. TEM micrographs B~[11-23] α . Sample irradiated at 430°C, 2.1 dpa, a) precipitates in bright field, b) one variant in dark field. Sample irradiated at 430°C, 0.4 dpa, c) precipitates in bright field, d) one variant in dark field.

At the doses of 1.5 dpa, the diffraction patterns confirmed the presence of small irradiation-induced precipitates (Figure 15) after irradiation at 300°C. These precipitates were hardly observable in bright field imaging (Figure 15a), but are clearly visible and can be counted in dark field imaging (Figure 15b). At the dose of 1 dpa, after irradiation at 300°C, the particle spots are hardly discernable on the diffraction patterns and the precipitates are not observable without a cleaning of the contamination by PIPS 2. A measurement in such micrographs (Figure 15c and f) is very imprecise and APT measurements are welcome. At the dose of 0.4 dpa, after irradiation at 300°C, neither the characteristic spots on the diffraction patterns, nor the particles on the micrograph can be distinguished, even after a cleaning by PIPS 2. APT analyses are needed. The APT technique, by a very fine chemical analysis, evidenced the precipitates at the irradiation temperature of 300°C as soon as the dose of 0.4 dpa. As an example, a 3D reconstruction of the vanadium, aluminum and titanium distribution in the α matrix of the Ti64 alloy after irradiation at the doses of 1 dpa at the temperatures of 300°C and 430°C, and 0.4 dpa at the temperature of 300°C is provided in Figure 16. The precipitates are highlighted by additional isosurfaces in the vanadium distributions. In this figure can be noticed the bigger size of the precipitates after irradiation at 430°C compared to the irradiation at 300°C, as observed by TEM. In Figure 16, the particles seem to have a lower size at the dose of 0.4 dpa than at the dose of 1 dpa after irradiation at 300°C. This can explain why TEM evidenced the particles at the dose of 1 dpa and did not at the dose of 0.4 dpa after irradiation at 300°C.

In Table 9 is detailed the measurement of the precipitates after irradiation at the temperature of 300°C, by TEM and APT. In spite of the difficulty to measure the particles by TEM, it appears a very good agreement in the size of the particles measured by TEM and APT. The measure reveals a small but significant increase in the size of the particles between 0.4 and 1.5 dpa, and a slightly higher density of the precipitates at the lower dose. The dose of 2 dpa was obtained during a previous irradiation campaign and seems to be not directly comparable to that of 0.4-

1.5 dpa. Notably, the precipitates appeared smaller after irradiation at the dose of 2 dpa than after irradiation at the dose of 1.5 dpa. In addition, the spots corresponding to the precipitates were hardly observable on the diffraction patterns after irradiation at the dose of 2 dpa. For this reason, the measurement in dark field imaging at the dose of 2 dpa was not easy and the particles were roughly measured and counted in bright field micrographs. It was not possible in these imaging conditions to be sure that only one variant was in contrast. This explains the uncertainty in the density at this dose (Table 9).

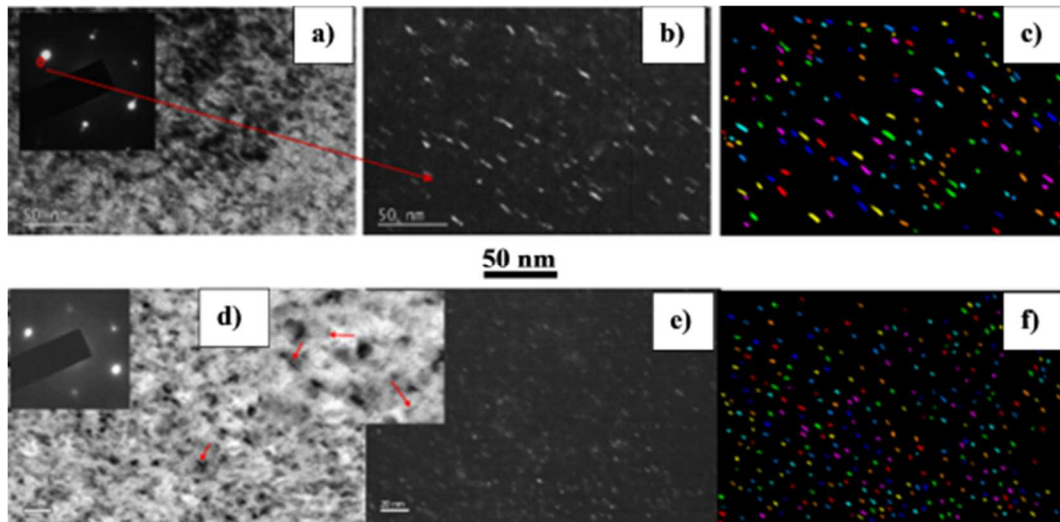


Figure 15. Radiation-induced precipitates in Ti64 irradiated at 300°C, B~[11-23] α , 1.5 dpa without PIPS 2, a) Bright Field, b) Dark Field, c) Visilog computing. 1 dpa with PIPS 2, d) Bright Field, e) Dark Field, f) Visilog computing.

Table 9. Quantitative measurement of the precipitates in the 300°C irradiation conditions (L=length, W=width, d=number density, V=analyzed volume), orientations B~[11-23], Magnification 100K. Comparison with APT.

Dose (dpa)	TEM				APT		
	L (nm)	W (nm)	d (10^{23} m^{-3})	V(m^{-3})	L (nm)	d (10^{23} m^{-3})	V(m^{-3})
2 ³	~4.3	~1.3	6-12	2.7×10^{-22}	4.3	10.7	-
1.5	5.4 ± 0.1	2.0 ± 0.1	26 ± 3	9.4×10^{-21}	-	-	-
1+PIPS 2	~3.6	~1.3	~4	5×10^{-21}	3.9	10.5	1.6×10^{-21}
0.4+PIPS 2	no	no	no	-	3.5	13	1×10^{-21}

³ Irradiation carried out in 2014

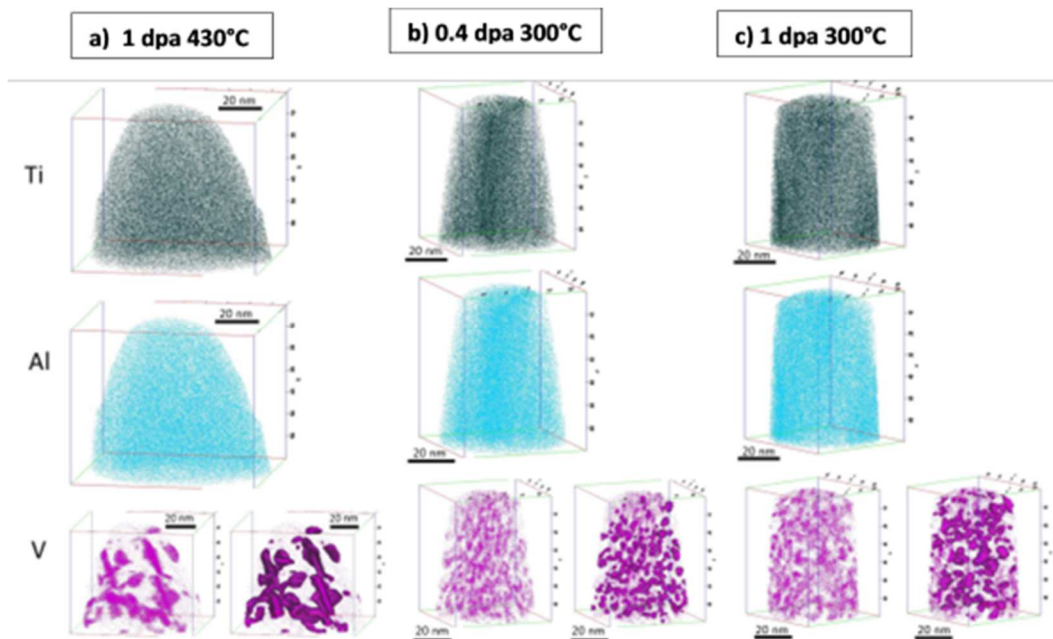


Figure 16. Needle tip 3D reconstruction (APT analysis). Spatial distribution of titanium, aluminum and vanadium in Ti64 alloy irradiated at the dose of 1, at the temperature of a) 430°C, c) 300°C and b) 0.4 dpa at 300°C.

5. Discussion

5.1. Introduction

Irradiation produces a great density of point defects (PDs), vacancies and self-interstitial atoms, in displacement cascades. Then PDs can be annihilated either by mutual recombination or by diffusion to the sinks. The remaining PDs can create bigger defects (clusters, precipitates, loops), inside the cascades thanks to particle shocks, or outside the cascades thanks to diffusion and segregation phenomena. At high temperature the diffusion processes take a significant part in the annihilation or in the segregation of PDs. At low temperatures vacancies are immobile, PDs are annihilated mainly in the cascades by mutual recombination. The diffusion and segregation processes are very low and the defects are mainly due to displacement cascades [10,30].

5.2. <a>-type defects

The microstructure observed here with <a>-loops and tangled dislocations after irradiation at 430 and 300°C seems to correspond to the “high-temperature regime” described by Zinkle et al. for austenitic stainless steels [31]. In this regime, loops are formed at low dose and approach a maximum density after a damage level of a few dpa, as observed here. The PDs are mobile and diffuse to be annihilated at sinks or agglomerate into bigger defects. In this regime, raising the irradiation temperature induces a lowering of the defect super-saturation [30], enhances mutual recombination or annihilation to the sinks thanks to faster diffusion processes [32] and thus reduces the loop nucleation incidence. In addition, it enhances the diffusivity of the species and promotes loop growth. Therefore, in this “high temperature regime” the size and density of the defects are dependent on the temperature. This explains the rise in size and the lowering in density of the <a>-loops in the 430°C irradiated specimen compared to the specimen irradiated at 300°C.

After irradiation at 600°C, the <a>-type microstructure dominated by tangled dislocations seems characteristic of the “very high temperature regime” [31]. In this “very high temperature regime”, loops are stated to form at low doses, and then to grow and to interact to form network dislocations [31].

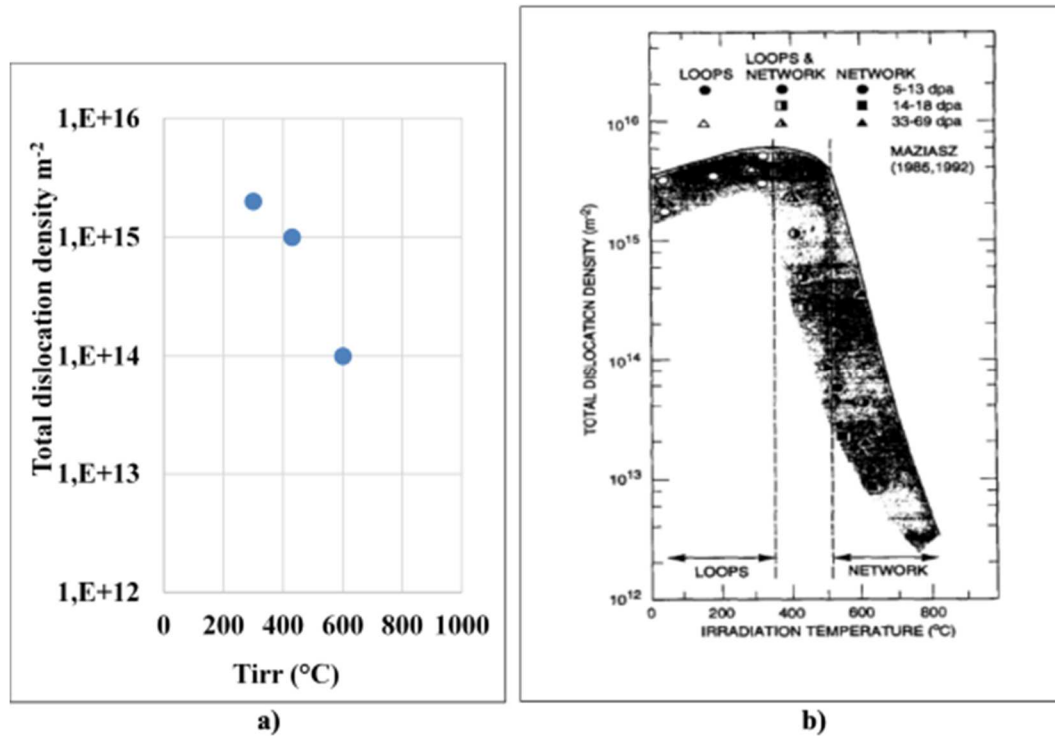


Figure 17. Linear density of the dislocations+loops versus irradiation temperature a) the present study at the dose of ~2 dpa, b) from Zinkle et al. for austenitic stainless steel [31].

Figure 17 illustrates the linear density of the dislocations + loops versus irradiation temperature in the present study at the dose of ~2 dpa (Figure 17a) and from Zinkle et al. for austenitic stainless steels (Figure 17b) [31]. The similarity of the two curves is worth being underlined. In the curve from Zinkle et al. appears, in addition, a “low temperature regime” dominated by a high density of “black dots” and small loops. In this domain the vacancies are not very mobile. The irradiation defect density and size are relatively insensitive to the dose and to the temperature and reach a saturation at a relatively low dose. This domain seems to be not observed in this study.

5.3. Radiation induced precipitates

The formation of the β precipitates results from the decomposition of the supersaturated α phase accelerated by irradiation. In previous studies [1,2,7,11] the precipitation and growth of the particles were attributed to the Radiation Induced Segregation phenomenon (RIS) [30,33,34] for irradiation temperatures ranging from 430 to 600°C. Because the diffusion of vacancies induces a solute flux in the opposite direction, solute elements that diffuse the most rapidly will be depleted at sinks (grain boundaries, dislocations, sub-grains, cavities and interfaces). On the contrary, slower diffusers will segregate at sinks. That comes from the inverse Kirkendall effect [10,35]. In addition, the interstitial diffusion to the sinks conducts to the diffusion of small size

solutes by a dragging effect phenomenon and can conduct to local segregations of these solutes at sinks.

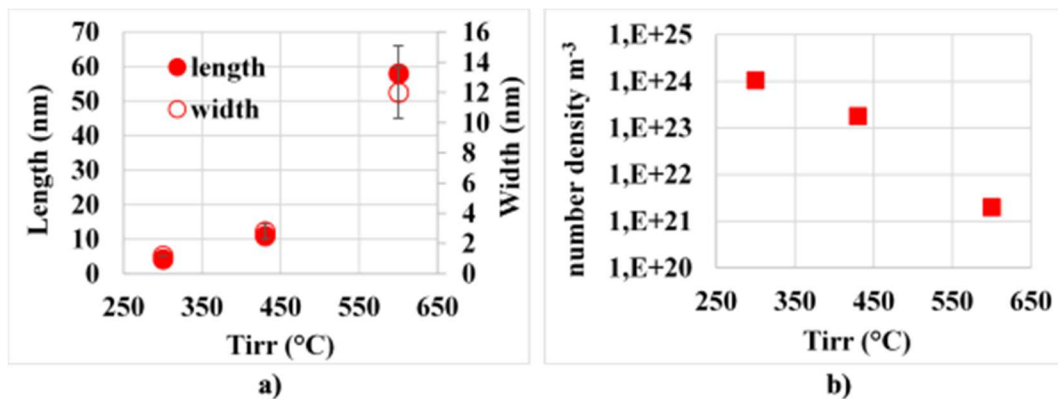


Figure 18: a) Size, b) number density of the radiation-induced precipitates versus irradiation temperature for the dose of ~2 dpa. Particles were measured by TEM at the temperatures of 430°C and 600°C and were measured by APT at the temperature of 300°C for a better precision.

For these reasons, the RIS usually leads to the nucleation of particles rich in slow-diffuser and small-sized solutes. The radiation-induced particles are niobium rich and meet this condition for the three irradiation temperatures. In addition, the RIS mechanism based on diffusion phenomena, is thermally dependent. When the irradiation temperature decreases, the diffusing length and velocity of punctual defects decrease, thus one expects a higher nucleation rate and a slower growth of the precipitates. The rise in the precipitate size (Figure 18a) associated with a lowering of their density (Figure 18b) with a rise in the irradiation temperature was evidenced here and was also observed by different authors [1,9,11,12]. The RIS phenomenon usually supposes a heterogeneous nucleation on PD sinks (grain boundaries, dislocations, sub-grains). This point was observed before with reinforced nucleation of precipitates on native dislocations after irradiation at 430°C and low flux [1]. It was confirmed here by the heterogeneous nucleation of precipitates on native dislocations, observed in a <a>-loop deprived zone, after irradiation at 430°C (Figure 19). Heterogeneous nucleation of particles was also observed on sub-grain after irradiation at 600°C (Figure 20a), and on a dislocation after irradiation at 300°C (arrowed Figure 20b). After irradiation at 430°C, the radiation-induced particles were observed not only on the native dislocation network but also in the α matrix with a uniform spatial distribution similar to that of the <a>-type loops (Figure 19). This confirms that <a> loops are good candidates to be nucleation sites for the precipitates, as suspected before [1], and can explain the quite uniform spatial distribution of the precipitates after irradiation at 430 and 300°C. Finely, according to some authors [12], the RIS mechanism supposes a thermodynamic equilibrium composition for the particles. This point was not measured here but was checked before, after irradiation at 430°C [1].

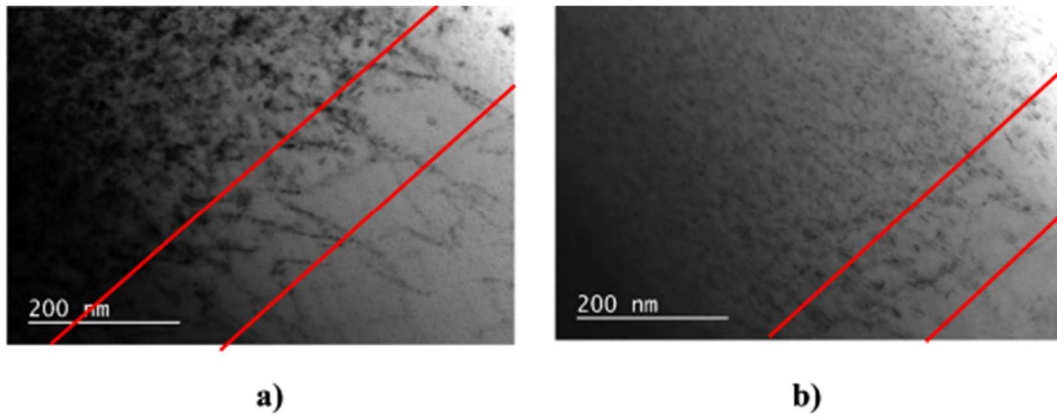


Figure 19. FIB thin foil of the sample irradiated at the temperature of 430°C and at the dose of 2 dpa, a) $\langle a \rangle$ -loops and precipitates, $g=10-11$, $B \sim [1-210]$, b) radiation-induced precipitates, $g=0002$, $B \sim [1-210]$. Area located at the bottom of the irradiated zone, at about 1.6 μm from the irradiated surface (see Figure 5). The area between the red straight lines is $\langle a \rangle$ -loop deprived and shows heterogeneous nucleation of precipitates on native dislocations. The area above the red lines show homogeneous nucleation of both precipitates and $\langle a \rangle$ -loops.

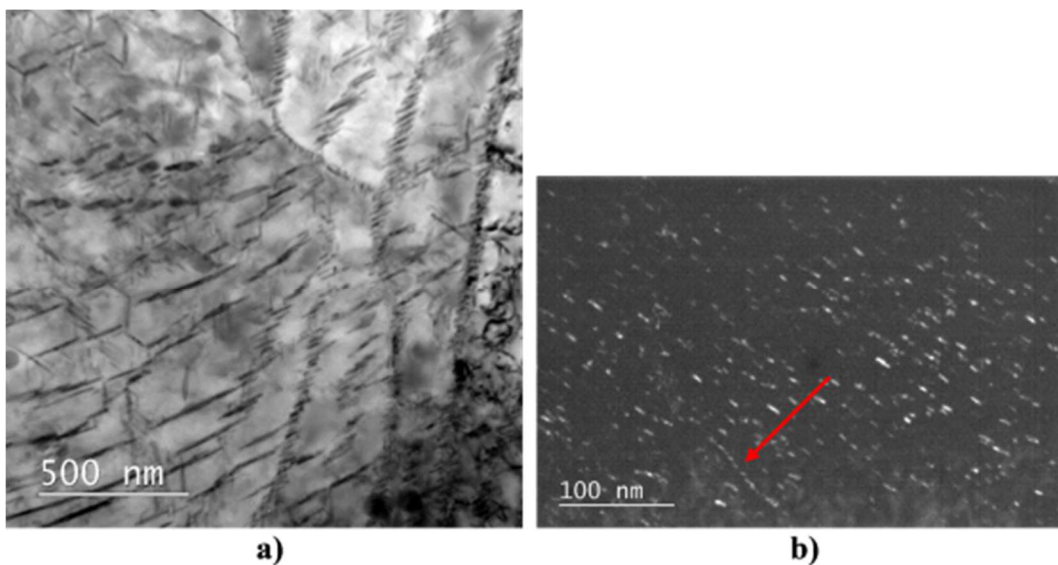


Figure 20. Heterogeneous nucleation of radiation induced precipitates, a) on laths and sub-grains after irradiation at 600°C, b) on a dislocation (arrowed) after irradiation at 300°C.

The RIS is expected in the temperature/flux domain of the present irradiations at 430°C and 600°C [10,30]. On the contrary, the RIS was not expected in the temperature/flux domain of the present irradiations at 300°C, because at low temperatures the diffusion and segregation processes are very low and the defects are mainly due to displacement cascades [10,30]. Nevertheless, the temperature/flux conditions at 300°C are not very far from the theoretical frontier of the RIS domain (calculated from the fusion temperature). Furthermore the Figure 17 tends to demonstrate that irradiation at the temperature of 300°C was situated in the “high temperature domain”, and not in the “low temperature domain” where the defects are mainly due to displacement cascades. In addition, in the “low temperature domain”, the size and density

of the particles are relatively insensible to the dose and to the temperature that is not the case here. Thus, the RIS phenomenon seems to occur not only during irradiation at 430°C and 600°C but also during irradiation at 300°C. The effective frontier for RIS seems to be at lower temperatures than predicted.

The RIS involves a nucleation and growth process [1]. This process induces a phase of quick rise in the number density of the particles, at low doses. Then comes a rise of the particle size without any change in their density. Finally, a steady state is reached without any change in the size and density of the particles. At higher temperature (430°C) the diffusion process is quicker and it can be assumed that the steady state will be reached at a lower dose than at 300°C. This could explain why the particle size is dose-dependent between 0.4 and 1.5 dpa after irradiation at 300°C and is independent of the dose after irradiation at 430°C (for doses higher than 0.4 dpa).

6. Conclusion

A method to image and count the precipitates was successfully developed with samples irradiated by ions at the temperature of 600°C, where the irradiation induced precipitates were easy to evidence. Indeed, the microstructure of the sample irradiated 2 dpa at 600°C was characterized by a low density of tangled dislocations ($\sim 10^{14}$ m/m³), and large precipitates (L~50 nm, $d\sim 2\times 10^{21}$ m⁻³). Then the process was applied for samples irradiated with ions at 430°C and 300°C characterized by a microstructure of tangled dislocations, loops and small precipitates.

It appeared that, in irradiation condition at 430°C, the precipitate measurement in dark field imaging with the $B\sim[11-23]_{\alpha}$, $g=10-11$, orientation and with a high magnification micrograph, provided similar results than APT analyses (L~10 nm, $d\sim 1.5\times 10^{23}$ m⁻³), contrary to lower magnifications and $g=0002$ orientation. In irradiation condition at 300°C, the precipitates were imaged for the first time by TEM as soon as the dose of 1 dpa but were not observed at the dose of 0.4 dpa, contrary to APT analyses. The precipitates were so small (L~5 nm) and their density was so high ($\sim 10^{24}$ m⁻³) that the counting was very imprecise by TEM. APT analyses were needed for an accurate measurement. Both TEM and APT measures indicated a slight rise in the particle length with the dose (0.4 to 1.5 dpa) from ~3.5 nm to ~5.5 nm after irradiation at 300°C. Conversely, after irradiation at 430°C, the microstructure did not change after irradiation at the dose of 2 dpa compared to the microstructure at the dose of 0.4 dpa.

Finally, the results presented here seems to attribute the nucleation and growth of the particles to the Radiation Induced Segregation phenomenon (RIS) [30,36,37], not only during irradiation at 430°C and 600°C but also during irradiation at 300°C

Footnotes

¹ The β transus temperature of this alloy is $1000\pm 5^\circ\text{C}$.

² Dislocations supposed to be already present before irradiation

³ Irradiation carried out in 2014

Figure captions

Figure 1. (from ref. [1]). BSE-SEM micrograph of the as-received Ti64 titanium alloy (the α and β phases appear in grey and white, respectively).

Figure 2. Small arrays of short dislocations observed, a) in the lamellar phase α_λ , b) in the sub-grains of the nodular phase α_p + sub grains.

Figure 3. Heating sample holder with nano-indentation platelets and TEM thin foils.

Figure 4. Damage and implantation profile determined from SRIM simulation for irradiations carried out with Ti^{2+} ions at an energy of 6 MeV, using an aluminum foil degrader (0.8 μm thick) in front of the specimen called “0.4 dpa 300°C”. The part of the profile concerned by TEM observations thanks to electrolytic preparation is hatched and corresponds to a dose of ~ 0.4 dpa.

Figure 5. General view of the FIB thin foil. Sample irradiated at, a) 430°C at the dose of 2 dpa, b) 300 °C at the dose of 0.4 dpa.

Figure 6. Tangled $\langle a \rangle$ dislocations in the sample irradiated at the dose of 2 dpa and at the temperature of 600°C.

Figure 7. $\langle a \rangle$ -loops and black dots after irradiation at 430°C, $g=10\text{-}11$ $B\sim[1\text{-}210]$, a) 2.1 dpa, b) 0.4 dpa.

Figure 8. Native $\langle a \rangle$ dislocations in the 300°C irradiated samples, a) 0.4 dpa, $g=1\text{-}210$, b) 1 dpa, $g=10\text{-}11$, c) 1.5 dpa, $g=1\text{-}210$.

Figure 9. $\langle a \rangle$ -loops and black dots after irradiation at 300°C, $g=10\text{-}11$ $B\sim[1\text{-}210]$, a) 0.4 dpa (without PIPS 2), b) 1 dpa (without PIPS 2), c) 1.5 dpa (with PIPS 2), d) 2 dpa (without PIPS 2).

Figure 10. TEM micrographs of the 600°C, 2.2 dpa irradiated sample, a) $B\sim[1\text{-}213]$ without PIPS 2 (the six crystallographic variants are called V1 to V6 and are detailed in §4.1), b) $g=0002$ $B\sim[10\text{-}10]$, with PIPS 2.

Figure 11. TEM micrographs of the 600°C, 2.2 dpa irradiated sample, $g=0002$ $B\sim[10\text{-}10]$, a) before cleaning with PIPS 2, b) after cleaning with PIPS 2.

Figure 12. Superposition of, a) the experimental matrix and the theoretical precipitate diffraction patterns, $B=[11\text{-}23]_\alpha$, b) the experimental matrix and precipitate diffraction patterns $B\sim[11\text{-}23]_\alpha$, $B=[11\text{-}1]_\beta$ (V4).

Figure 13. TEM micrographs $B\sim[11\text{-}23]_\alpha$ $g=01\text{-}1\text{-}1$, a) bright field, b) diffraction pattern, c) V5 variant in dark field imaging, d) V4 variant in dark field imaging.

Figure 14. TEM micrographs $B\sim[11\text{-}23]_\alpha$. Sample irradiated at 430°C, 2.1 dpa, a) precipitates in bright field, b) one variant in dark field. Sample irradiated at 430°C, 0.4 dpa, c) precipitates in bright field, d) one variant in dark field.

Figure 15. Radiation-induced precipitates in Ti64 irradiated at 300°C, $B\sim[11-23]_{\alpha}$, 1.5 dpa without PIPS 2, a) Bright Field, b) Dark Field, c) Visilog computing. 1 dpa with PIPS 2, d) Bright Field, e) Dark Field, f) Visilog computing.

Figure 16. Needle tip 3D reconstruction (APT analysis). Spatial distribution of titanium, aluminum and vanadium in Ti64 alloy irradiated at the dose of 1, at the temperature of a) 430°C, c) 300°C and b) 0.4 dpa at 300°C.

Figure 17. Linear density of the dislocations+loops versus irradiation temperature, a) the present study at the dose of ~ 2 dpa, b) from Zinkle et al. for austenitic stainless steel [31].

Figure 18: a) Size, b) number density of the radiation-induced precipitates versus irradiation temperature for the dose of ~ 2 dpa. Particles were measured by TEM at the temperatures of 430°C and 600°C and were measured by APT at the temperature of 300°C for a better precision.

Figure 19. FIB thin foil of the sample irradiated at the temperature of 430°C and at the dose of 2 dpa, a) $\langle a \rangle$ -loops and precipitates, $g=10-11$, $B\sim[1-210]$, b) radiation-induced precipitates, $g=0002$, $B\sim[1-210]$. Area located at the bottom of the irradiated zone, at about 1.6 μm from the irradiated surface (see Figure 5). The area between the red straight lines is $\langle a \rangle$ -loop deprived and shows heterogeneous nucleation of precipitates on native dislocations. The area above the red lines show homogeneous nucleation of both precipitates and $\langle a \rangle$ -loops.

Figure 20. Heterogeneous nucleation of radiation induced precipitates, a) on laths and sub-grains after irradiation at 600°C, b) on a dislocation (arrowed) after irradiation at 300°C.

Acknowledgement:

The authors acknowledge the support of the French National Research Agency (ANR), under grant ANR-12-RMNP-0005 (project TESAMI, meaning Titanium and Its Alloys under Irradiation) and the partners of the project: Naval Group, CEA, TechnicAtom, TIMET, Neotiss, EVEA, ICB and SUBATECH.

The authors would like to warmly thank the staff of JANNuS facility for their assistance during ion irradiations.

The authors are grateful to Yvon Millet (TIMET Savoie) for the supply of a Ti64 bar.

This work received assistance from the “Agence Nationale de la Recherche” program GENESIS referenced as ANR-11-EQPX-0020 for the APT analyses.

Data availability statement

All data generated or analyzed during this study are included in this published article.

References

- [1] S. Doriot, E. Jouanny, J. Malaplate, F. Dalle, L. Allais, T. Millot, M. Descoins, D. Mangelinck, M. Dehmas, Evolution of defects in Ti6-4 under Ti²⁺ ion irradiation: focus on radiation-induced precipitates, *Journal of Nuclear Materials* 511 (2018) 264-276. <https://doi.org/10.1016/j.jnucmat.2018.09.027>.
- [2] R.H. Jones, L.A. Charlot, Microstructure of irradiated Ti-70A and Ti-6Al-4V, *J. Nucl. Mater.* 91 (1980) 329-335.
- [3] B.S. Rodchenkov, A.V. Koslov, Yu. G. Kuznetsov, G.M. Kalinin, Yu.S. Strebkov, Irradiation behaviour of titanium alloys for ITER blanket modules flexible attachment, *J. Nucl. Mater.* 307-311 (2002) 421-425. <https://doi.org/10.1016/j.jnucmat.2010.12.194>
- [4] B.K. Singh, V. Singh, Effect of fast neutron irradiation on tensile properties of AISI 304 stainless steel and alloy Ti-6Al-4V, *Mat. Sci. and Eng. A*, 528 (2011) 5336-5340. <https://doi.org/doi:10.1016/j.msea.2011.03.066>
- [5] D.R. Duncan, R.J. Puigh, E.K. Opperman, Titanium alloy tensile properties after neutron irradiation, *J. Nucl. Mater.* 103-104 (1981) 919-924.
- [6] O.A. Kozhenikov, E.V. Nesterova, V.V. Rybin, I.I. Yarmolovich, Influence of neutron irradiation on deformability and fracture micromechanisms of titanium α -alloys, *J. Nucl. Mater.* 271-272 (1999) 472-477.
- [7] S. Tähtinen, P. Moilanen, B.N. Singh, D. J. Edward, Tensile and fracture toughness properties of unirradiated and neutron irradiated titanium alloys, *J. Nucl. Mater.* 307-311 (2002) 416-420.
- [8] S. Tähtinen, P. Moilanen, B.N. Singh, Effect of displacement dose and irradiation temperature on tensile and fracture toughness properties of titanium alloys, *J. Nucl. Mater.* 367-370 (2007) 627-632. <https://doi.org/doi:10.1016/j.jnucmat.2007.03.042>.
- [9] P. Marmy, T. Legey, Impact of irradiation on the tensile and fatigue properties of two titanium alloys, *J. Nucl. Mater.* 296 (2001) 155-164.
- [10] G.S. Was, Irradiation-induced voids and bubbles, in: *Fundamentals of Radiation Materials Science*, Springer, Berlin, Heidelberg, New York, (2007) 388-390.
- [11] G. Ayrault, Radiation-induced precipitation in single- and dual-ion irradiated Ti-6Al-4V, *J. Nucl. Mater.* 113 (1983) 1-13.
- [12] D.L. Plumton, G.L. Kulcinski, R.A. Dodd, Radiation induced precipitation in 9 MeV Al ion irradiated Ti-6Al-4V, *J. Nucl. Mater.* 144 (1987) 264-274.
- [13] D.L. Plumton, G.L. Kulcinski, R.A. Dodd, Phase transformations in ion irradiated Ti-6242s, *J. Nucl. Mater.* 144 (1987) 252-263.
- [14] S.C. Agarwal, G. Ayrault, D.I. Potter, A. Taylor, F.V. Nolfi, Microstructure of single and dual-ion irradiated Fe-20Ni-15Cr and Ti-6Al-4V alloys, *J. Nucl. Mater.* 85-86 (1979) 653-657.
- [15] Peng Jin, Tie-Long Shen, Jing Li, Yu-Shan Yang, Chao Liu, Ming-Huan Cui, "Changes in the microstructure and mechanical properties of Ti-6Al-4V alloys induced by Fe ion irradiation at a high He generation rate", *Vacuum* 207 (2023) 111639, <https://doi.org/10.1016/j.vacuum.2022.111639>.
Received 18 July 2022; Received in revised form 13 October 2022; Accepted 25 October 2022
- [16] T. Leguey, R. Schäublin, P. Marmy, M. Victoria, Microstructure of Ti5Al2.5Sn and Ti6Al4V deformed in tensile and fatigue tests, *J. Nucl. Mater.* 305 (2002) 52-59.
- [17] G. Lütjering, Property optimization through microstructural control in titanium and aluminum alloys, *Mater. Sci. Eng.* 263 (1999) 117-126.
- [18] P. Castany, F. Pettinari-Sturmelt, J. Crestou, J. Douin, A. Coujou, Experimental study of dislocation mobility in a Ti-6Al-4V alloy, *Acta Mater.* 55 (2007) 6284-6291. <https://doi.org/doi:10.1016/j.actamat.2007.07.032>.
- [19] E. Jouanny, S. Doriot, J. Malaplate, M. Dehmas, L. Allais, M. Le Thuaut, T. Millot, Evolution of defects in titanium grade 2 under Ti²⁺ ion irradiation, *J. Microsc.* 255 (3) (2017) 275-286. <https://doi.org/10.1111/jmi.12499>.
- [20] L. K. Mansur, Correlation of neutron and heavy-ion damage: II. The predicted temperature shift if swelling with changes in radiation dose rate, *J. Nucl. Mater.* 78 (1978) 156-160.
- [21] S. Pellegrino et. al., Ion irradiation and radiation effect characterization at the JANNuS-Saclay triple beam facility, *J. Mater. Res.* 30 (2015) 1183-1194.
- [22] Y. Serruys, P. Trocelier S. Miro, E. Bordas, M.-O. Ruault, O. Kaitasov, S. Henry, O. Leseigneur, T. Bonnaille, S. Pellegrino, S. Vaubailon, D. Uriot, JANNuS : A multi-irradiation platform for experimental validation at the scale of the atomistic modeling, *J. Nucl. Mater.* 386-388 (2009) 967-970. <https://doi.org/10.1016/j.jnucmat.2008.12.262>
- [23] A. Gentils, C. Cabet, Investigating radiation damage in nuclear energy materials using JANNuS multiple ion beams, *Nucl. Inst. Met. Phys. Res. B* 447 (2019) 107 DOI : 10.1016/j.nimb.2019.03.039
- [24] R.F. Egerton, *Electron Energy-Loss Spectroscopy in the Electron Microscope*, Second Edition, Plenum Press, New York, 1996.
- [25] P.A. Crozier, Measurement of inelastic electron scattering cross sections by electron energy-loss spectroscopy, *Philos. Mag.* 61 (1990) 331-336.

-
- [26] D.R.G. Mitchell, Determination of mean free path for energy loss and surface oxide film thickness using convergent beam electron diffraction and thickness mapping : A case study using Si and P91 steel, *J. Microsc.* 224 (2006) 187-196.
- [27] C.W. Lee, Y. Ikematsu, D. Shindo, Measurement of mean free paths for inelastic electron scattering of Si and SiO₂, *J. Electr. Microsc.* 51 (3) (2002) 143-148.
- [28] W.C. Burgers, On the process of transition of the cubic-body-centered modification into the hexagonal-close-packed modification of zirconium, *Phys.* 1 (nd) 561-586.1934
- [29] P. Wilkes, G.L. Kulsinski, Heavy ion irradiation of a Ti-6Al-4V alloy, *J. Nucl. Mater.* 206 (1978) 427-430.
- [30] M. Nastar, F. Soisson, *Comprehensive Nuclear Materials 1 : Basic Aspects of radiation effects in solids / Basic aspects of multi-scale modeling* (2012) 471-496. Elsevier.
- [31] S.J. Zinkle, P.J. Maziasz, R.E. Stoller, Dose dependence of the microstructural evolution in neutron-irradiated austenitic stainless steel, *J. Nucl. Mater.* 206 (1993) 266-286.
- [32] M. Griffiths, D. Faulkner, R.C. Styles, Neutron damage in α -titanium, *J. Nucl. Mater.* 119 (1983) 189-207.
- [33] P.R. Okamoto, L.E. Rehn, L.E. Rehn, Radiation-induced segregation in binary and ternary alloys, *J. Nucl. Mater.* 83 (1979) 2-23.
- [34] R. Cauvin, G. Martin, Radiation induced homogeneous precipitation in undersaturated solid-solutions, *J. Nucl. Mater.* 83 (1979) 67-78.
- [35] K. Nordlund and R.S. Averback, Inverse kirkendal mixing in collision cascades, *Physical Review B*, 59 (1999) 20-23.
- [36] P.R. Okamoto, L.E. Rehn, L.E. Rehn, Radiation-induced segregation in binary and ternary alloys, *J. Nucl. Mater.* 83 (1979) 2-23.
- [37] R. Cauvin, G. Martin, Radiation induced homogeneous precipitation in undersaturated solid-solutions, *J. Nucl. Mater.* 83 (1979) 67-78.